

PHYSICAL PROPERTIES OF THE CIRCUMNUCLEAR STARBURST RING IN THE BARRED GALAXY NGC 1097

PEI-YING HSIEH^{1,2}, SATOKI MATSUSHITA^{2,7}, GUILIN LIU³, PAUL T. P. HO^{2,6}, NAGISA OI⁴, AND YA-LIN WU^{2,5},
 PYHSIEH@ASIAA.SINICA.EDU.TW

¹ Institute of Astrophysics, National Central University, No.300, Jhongda Rd., Jhongli City, Taoyuan County 32001, Taiwan, R.O.C.

² Academia Sinica Institute of Astronomy and Astrophysics, P.O. Box 23-141, Taipei 10617, Taiwan, R.O.C.

³ Astronomy Department, University of Massachusetts, Amherst, MA 01003, USA

⁴ Department of Astronomy, School of Science, Graduate University for Advanced Studies, 2-21-1 Osawa, Mitaka, Tokyo 181-8588, Japan

⁵ Institute of Astrophysics, National Taiwan University, No. 1, Sec. 4, Roosevelt Road, Taipei 10617, Taiwan, R.O.C.

⁶ Harvard-Smithsonian Center for Astrophysics, 60 Garden Street, Cambridge, MA 02138, USA and

⁷ Joint ALMA Office, Alonso de Córdova 3107, Vitacura 763 0355, Santiago, Chile

Accepted for publication in ApJ

ABSTRACT

We report high resolution $^{12}\text{CO}(J = 2-1)$, $^{13}\text{CO}(J = 2-1)$, and $^{12}\text{CO}(J = 3-2)$ imaging of the Seyfert 1/starburst ring galaxy NGC 1097 with the Submillimeter Array to study the physical and kinematic properties of the 1-kpc circumnuclear starburst ring. Individual star clusters as detected in the HST map of Pa α line emission have been used to determine the star formation rate, and are compared with the properties of the molecular gas. The molecular ring has been resolved into individual clumps at GMA-scale of 200–300 pc in all three CO lines. The intersection between the dust lanes and the starburst ring, which is associated with orbit-crowding region, is resolved into two physically/kinematically distinct features in the $1''.5 \times 1''.0$ (105×70 pc) $^{12}\text{CO}(J = 2-1)$ map. The clumps associated with the dust lanes have broader line width, higher surface gas density, and lower star formation rate, while the narrow line clumps associated with the starburst ring have opposite characteristics. Toomre-Q value under unity at the radius of the ring suggests that the molecular ring is gravitationally unstable to fragment at the scale of the GMA. The line widths and surface density of gas mass of the clumps show an azimuthal variation related to the large scale dynamics. The star formation rate, on the other hand, is not significantly affected by the dynamics, but has a correlation with the intensity ratio of $^{12}\text{CO}(J = 3-2)$ and $^{12}\text{CO}(J = 2-1)$, which traces the denser gas associated with star formation. Our resolved CO map, especially in the orbit-crowding region, for the first time demonstrates observationally that the physical/kinematic properties of the GMAs are affected by the large scale bar-potential dynamics in NGC 1097.

Subject headings: Galaxies: individual (NGC 1097) – Galaxies: ISM – Galaxies: Seyfert – Galaxies: starburst – radio lines: ISM – Submillimeter: ISM

1. INTRODUCTION

NGC 1097 [SB(s)b; de Vaucouleurs et al. 1991] is a nearby ($D = 14.5$ Mpc; $1'' = 70$ pc, Tully 1988) barred spiral galaxy. A pair of dust lanes are located at the leading edges of the major bar. A radio continuum image at 1.465 GHz shows faint ridges coinciding with the dust lanes (Hummel et al. 1987). The nucleus is thought to be a transition object from LINER to Seyfert 1 (Storchi-Bergmann et al. 2003). Detailed studies on the nucleus show morphological and kinematic evidences of the nuclear spirals on the order of 30 pc, and was interpreted as part of the fueling chain to the very center (Fathi et al. 2006; Davies et al. 2009; van de Ven & Fathi 2010). NGC 1097 is also an IRAS bright galaxy (Sanders et al. 2003). The contribution of large amount of IR flux arise from its 1 kpc-circumnuclear starburst ring (e.g., Hummel et al. 1987; Telesco & Gatley 1981; Kotilainen et al. 2000). The starburst ring hosts “hot-spots” composed with super star clusters identified in HST images (Barth et al. 1995), and was suggested to have an instantaneous burst of star formation which occurred $\sim 6-7$ Myr ago (Kotilainen et al. 2000).

The molecular gas of NGC 1097 in the nuclear region

has been previously mapped in the dense gas tracer of $\text{HCN}(J = 1-0)$, low excitation lines of $^{12}\text{CO}(J = 1-0)$ and $^{12}\text{CO}(J = 2-1)$ (Kohno et al. 2003; Hsieh et al. 2008, hereafter Paper I). These maps show a central concentration coincident with the peak of the 6-cm radio continuum core (Hummel et al. 1987), as well as a molecular ring coincident with the starburst ring. A pair of molecular ridges coincident with the dust lanes are also detected, and show non-circular motions, possibly caused by the bar-potential dynamics (e.g., Athanassoula 1992a,b). The molecular ring has a typical warm temperature ($T_K \sim 100$ K) and denser gas ($n_{\text{H}_2} \sim 10^3 \text{ cm}^{-3}$) consistent with the starburst environments (Wild et al. 1992; Aalto et al. 1995). The molecular ring exhibits a twin-peak structure in the $4''-10''$ resolution interferometric CO and HCN maps, where a pair of molecular concentrations are located in the intersection of the molecular dust lanes and the star forming ring. Its orientation is nearly perpendicular to the stellar bar. The twin-peak has higher H_2 column density than the surrounding ring, and similar features have been seen in other barred galaxies, and can be explained by the crowding of gas streamlines (e.g., Kenney et al. 1992; Reynaud & Downes 1997; Kohno et al. 1999). The

gas flow gradually changes direction and migrates toward the center of the galaxy to accumulate to form a ring (Schwarz 1984; Athanassoula 1992b; Piner et al. 1995). Subsequent enhanced star formation may occur through gravitational fragmentation stochastically (Elmegreen 1994), or dynamically driven by collision of molecular clouds (Combes & Gerin 1985), or alternatively originated from the shock compressed gas near the contact point of the dust lanes and the ring (Böker et al. 2008). Another intriguing topic is thus whether the occurrence of the circumnuclear starburst ring would prohibit or boost its nuclear activities (e.g., Telesco et al. 1993; Scoville et al. 1985; Heckman 1991; Ho et al. 1997).

High spatial/kinematic resolution observations of molecular lines are essential to study the circumnuclear ring structures, since they are the sites of star formation and respond to the large scale dynamics. NGC 1097 is one of the best example to study the circumnuclear ring for its typical structures of dust lanes, starburst ring, and nuclear activities. In order to study the physical and kinematic properties of the starburst ring, especially in the twin-peak region, we have now obtained higher resolution $^{12}\text{CO}(J = 2-1)$ ($1''.5 \times 1''.0$), $^{13}\text{CO}(J = 2-1)$ ($1''.8 \times 1''.4$), and $^{12}\text{CO}(J = 3-2)$ ($3''.5 \times 2''.1$) maps down to 100 pc. By virtue of the high angular resolution multi-J lines, we derive the fundamental properties of molecular gas as well as star formation in the ring in order to give a comprehensive view of this system.

2. OBSERVATIONS AND DATA REDUCTION

2.1. SMA observations

We observed NGC 1097 with the Submillimeter Array¹ (Ho et al. 2004) at the summit of Mauna Kea, Hawaii. The array consists of eight 6-m antennas. Four basic configurations of the antennas are available. With the compact configuration, two nights of $^{12}\text{CO}(J = 2-1)$ data were obtained in 2004 (Paper I). To achieve higher spatial resolution, we obtained two further nights of $^{12}\text{CO}(J = 2-1)$ data with the extended and the very extended configurations in 2005. To study the excitation of the gas, we also obtained one night of $^{12}\text{CO}(J = 3-2)$ data in 2006 with the compact configuration. All the observations have the same phase center. We located the phase center at the 6-cm peak of the nucleus (Hummel et al. 1987). Detailed observational parameters, sky conditions, system performances, and calibration sources are summarized in Table 1.

The SMA correlator processes two IF sidebands separated by 10 GHz, with ~ 2 GHz bandwidth each. The upper/lower sidebands are divided into slightly overlapping 24 chunks of 104 MHz width. With the advantage of this wide bandwidth of the SMA correlator, the receivers were tuned to simultaneously detect three CO lines in the 230 GHz band. The $^{12}\text{CO}(J = 2-1)$ line was set to be in the upper sideband, while the $^{13}\text{CO}(J = 2-1)$ and the $\text{C}^{18}\text{O}(J = 2-1)$ lines were set to be in the lower sideband. For the $^{12}\text{CO}(J = 3-2)$ line, we placed the redshifted frequency of 344.35 GHz in the upper sideband.

We calibrated the SMA data with the MIR-IDL software package. The detailed calibration procedures of the data of compact configuration were described in Paper I. For the extended and very extended configurations, where Uranus is resolved quite severely, we observed two bright quasars (3C454.3 & 3C111), and adopted a similar bandpass/flux calibration method as described in Paper I. At 345 GHz, we used both Uranus and Neptune for the flux and bandpass calibrators.

Mapping and analysis were done with the MIRIAD and NRAO AIPS packages. The visibility data were CLEANed in AIPS by task IMAGR. We performed the CLEAN process to deconvolve the dirty image to clean image. The deconvolution procedure was adopted with the Högbom algorithm (Högbom 1974) and the Clark algorithm (Clark 1980). We used a loop gain of 10% and did restrict the CLEAN area by iterative examinations. The CLEAN iterations were typically stopped at the 1.5σ residual levels. The number of CLEAN components in individual channel maps was typically about 300.

All of the 230 GHz visibility data were combined to achieve a better uv coverage and sensitivity. Our 230 GHz continuum data were constructed by averaging the line-free channels. Due to the sideband leakage at 230 GHz, a limited bandwidth of 1.3 GHz and 0.5 GHz were obtained respectively in the upper and lower sidebands to make a continuum image. Weak continuum emission at 230 GHz with a peak intensity of 10 mJy beam^{-1} was detected at about 4σ at the southern part of the ring. The 1σ noise level of the continuum emission at 345 GHz averaged over the line-free bandwidth of 0.4 GHz is 6 mJy beam^{-1} , and there is an $\sim 3\sigma$ detection in the nucleus and in the ring. In this paper we did not subtract the continuum emission since it is too faint as compared to the noise level in the line maps. The spectral line data of $^{12}\text{CO}(J = 2-1)$ and $^{12}\text{CO}(J = 3-2)$ were binned to 10 km s^{-1} resolution. As the $^{13}\text{CO}(J = 2-1)$ emission is fainter, those data were binned to 30 km s^{-1} resolution to increase the S/N. The $\text{C}^{18}\text{O}(J = 2-1)$ line emission was detected in the lower sideband of the 230 GHz data. However, the leakage from the $^{12}\text{CO}(J = 2-1)$ line in the upper sideband was significant. Therefore, in this paper we will not make use of the $\text{C}^{18}\text{O}(J = 2-1)$ data for further analysis. In this paper, we present the maps with natural weighting. The angular resolution and rms noise level per channel are $1''.5 \times 1''.0$ and 26 mJy beam^{-1} (400 mK) for the $^{12}\text{CO}(J = 2-1)$, $1''.8 \times 1''.4$ and 30 mJy beam^{-1} (320 mK) for the $^{13}\text{CO}(J = 2-1)$ data, and $3''.5 \times 2''.1$ and 35 mJy beam^{-1} (47 mK) for the $^{12}\text{CO}(J = 3-2)$ data. We used AIPS task MOMNT to construct the integrated intensity-weighted maps. The task would reject pixels lower than the threshold intensity, set to be $2.5-3\sigma$ in the CLEANed cube after smoothing in velocity and spatial direction. The smoothing kernels are 30 km s^{-1} in the velocity direction, and a factor of two of the synthesized beam in the spatial direction in the maps we made.

In the following line ratio analysis, we use the maps truncated to the same uv coverage as in Sect. 3.4.1

2.2. HST NICMOS Pa α image

¹ The SMA is a joint project between the Smithsonian Astrophysical Observatory and the Academia Sinica Institute of Astronomy and Astrophysics and is funded by the Smithsonian Institution and the Academia Sinica.

As one of the sample galaxies in the HST NICMOS survey of nearby galaxies (PI: Daniela Calzetti, GO: 11080), NGC 1097 was observed on November 15, 2007 by HST equipped with NIC3 camera. NIC3 images have a $51'' \times 51''$ field of view and a plate scale of $0''.2$ with an undersampled PSF. In this survey, each observation consists of images taken in two narrowband filters: one centered on the $\text{Pa}\alpha$ recombination line of hydrogen ($1.87 \mu\text{m}$) (F187N), and the other on the adjacent narrow-band continuum exposure (F190N), which provides a reliable continuum subtraction. Each set of exposures was made with a 7-position small ($< 1''$ step) dithered. Exposures of 160 and 192 seconds per dither position in F187N and F190N, respectively, reach a 1σ detection limit of $2.3 \times 10^{-16} \text{ erg s}^{-1} \text{ cm}^{-2} \text{ arcsec}^{-2}$ in the continuum-subtracted $\text{Pa}\alpha$ image of NGC 1097.

Using the STSDAS package of IRAF, we removed the NICMOS *Pedestal* effect, masked out bad pixels and cosmic rays, and drizzled the dither images onto a finer ($0''.1$ per pixel) grid frame. The resultant drizzled F190N image is then scaled and subtracted from its F187N peer after carefully aligning to the latter using foreground stars. The residual shading effect in the pure $\text{Pa}\alpha$ image is removed by subtracting the median of each column. This strategy works well for the NGC 1097 data which contain relatively sparse emission features. The PSF of the final $\text{Pa}\alpha$ image has a $0''.26$ FWHM. Further details of the data reduction and image processing are described in Liu et al. (2010a).

3. RESULTS

3.1. Morphologies of the molecular gas

The integrated intensity maps of $^{12}\text{CO}(J = 2-1)$, $^{12}\text{CO}(J = 3-2)$ and $^{13}\text{CO}(J = 2-1)$ lines are shown in Figure 1. The maps show a central concentration and a ring-like structure with a radius of 700 pc ($\sim 10''$). The gas distribution of $^{12}\text{CO}(J = 3-2)$ map is similar to that of the $^{12}\text{CO}(J = 2-1)$ map, where the central concentration has a higher integrated intensity than the ring. The $^{13}\text{CO}(J = 2-1)$ map, on the other hand, shows comparable intensity between the ring and the nucleus. Comparing with the previous observations (Paper I), the molecular ring and the central concentration have been resolved into individual clumps, especially for the twin-peak structure in the molecular ring, with the higher resolution $^{12}\text{CO}(J = 2-1)$ map. We also show the peak brightness temperature map of the $^{12}\text{CO}(J = 2-1)$ emission in Figure 1 made by the AIPS task SQASH to extract the maximum intensity along the velocity direction at each pixel. Note that the ring and the nucleus have comparable brightness temperatures.

The position of the AGN (6-cm radio continuum core; Hummel et al. 1987), which is assumed to be the dynamical center of the galaxy, seems to be offset by $0''.7$ northwest to the central peak of the integrated CO maps. This is also seen in our previous results and we interpreted it as a result of the intensity weighting in the integration (Paper I). To confirm if the dynamical center as derived from the $^{12}\text{CO}(J = 1-0)$ emission (Kohno et al. 2003) is consistent with that of $^{12}\text{CO}(J = 2-1)$, we will have some more analysis in Sect. 3.5.

In Figures 2 and 3, we show the $^{12}\text{CO}(J = 2-1)$ and $^{12}\text{CO}(J = 3-2)$ channel maps overlaid on the archival

HST I-band image (F814W) to show the gas distribution at different velocities. We show these images at the resolution of 40 km s^{-1} , but we use the resolution of 10 km s^{-1} for actual analysis. The astrometry of the HST I-band image was corrected by the known positions of the foreground 19 stars in the catalog of USNO-A 2.0. After astrometry correction, we found the intensity peak of the nucleus of HST image has a $0''.8$ offset northeast to the position of AGN, this may be due to extinction, or inaccurate astrometry. We can not rule out these factors. However this offset is within the uncertainty of the CO synthesized beam. Both ^{12}CO transitions show emission with a total velocity extent of $\sim 550\text{--}600 \text{ km s}^{-1}$ at the 2σ intensity level. The western molecular ridge/arms (coincident with the dust lane in the optical image) joins the southwestern part of the ring from -162 km s^{-1} to 37 km s^{-1} , and the eastern molecular ridge joins the northeast ring from -42 km s^{-1} to 157 km s^{-1} . We find that the velocity extent of these ridges is $\sim 200 \text{ km s}^{-1}$ at the 2σ intensity level. In between the molecular ring and the nuclear disk, there are also extended ridge emission connecting the nuclear disk and the ring in both lines. This ridge emission is more significant in the $^{12}\text{CO}(J = 2-1)$ than in the $^{12}\text{CO}(J = 3-2)$ map. However, this may be an angular resolution effect. The ridge emission looks more significant in the $^{12}\text{CO}(J = 2-1)$ map, but the ridge emission does not have enough flux density (Jy/beam) to reach the same S/N in the high resolution image, which means it has extended structure, i.e., the faint ridge emission in the high resolution map is more or less resolved.

In Figure 4, we show the $^{12}\text{CO}(J = 2-1)$ integrated intensity map overlaid on the HST I-band (F814W) archival image to compare the optical and radio morphologies. The $\text{Pa}\alpha$ image (near-IR) is also shown in Figure 4. The optical image shows a pair of spiral arms in the central 1 kpc region. The arms consist of dusty filaments and star clusters. Two dust lanes at the leading side of the major bar connect to the stellar arms. Dusty filaments can also be seen to be filling the area between the spiral arms and the nucleus. The $^{12}\text{CO}(J = 2-1)$ map ($1''.5 \times 1''.0$) shows a central concentration, a molecular ring and molecular ridges with good general correspondence to the optical image. However, there are significant differences in a detailed comparison. Although the starburst ring looks like spiral arms in the optical image, the molecular gas shows a more complete ring, and the molecular ridges are seen to join the ring smoothly. Inside of the stellar ring, the major dust lanes are offset from the molecular ring. Assuming that the ^{12}CO emission is faithfully tracing the total mass, the prominent dark dust lanes are not significant features while they join the molecular ridges as the edge of the ring. The stellar ring or star formation activities are then correlated with the peaks in the total mass distribution. The central molecular concentration corresponds in general with the stellar nucleus, but is offset to the south of the stellar light. The nuclear molecular distribution is quite asymmetric with lots of protrusions at the lower intensity contours, which may correspond to gas and dust filaments which connect the nuclear concentration to the molecular ring.

3.2. Properties of the molecular gas

The molecular ring has been resolved into a complex structure of compact sources immersed in a diffuse emission with lower surface brightness as shown in Figure 1. At our resolution (100 pc), the contrast between clumps and diffuse emission is not high. Hence, the clumps are possibly connected to each other via the diffuse emission. With such a physical configuration, it is difficult to uniquely isolate the individual clumps by some clump finding algorithm (e.g., Williams et al. 1994). Moreover, the detection of clumps is dependent on the angular resolution which is available. In this paper, we select the peaks of the main structures in the $^{12}\text{CO}(J=2-1)$ integrated intensity map, in order to locate the individual clumps within the ring and the molecular ridges. We define the clumps located outside of the $10''$ radius as the dust lane clumps, and those within the $10''$ radius as the ring clumps.

The typical size of Giant Molecular Clouds (GMCs) is on the order of a few to few tens pc (Scoville et al. 1987). The size of the clumps in the ring of NGC 1097, as detected with our synthesized beam, is at least ~ 200 pc. We are therefore detecting molecular clumps larger than GMCs, most likely a group of GMCs, namely Giant Molecular Cloud Associations (GMAs; Vogel et al. 1998). Here we still use the term “clumps” to describe the individual peaks at the scale of GMA. We expect that the clumps would be resolved into individual GMCs when higher angular resolution is available. In Table 2, we show the quantities measured within one synthesized beam to study the kinematic properties with a high resolution (i.e., one synthesized beam) in the following sections. The observed peak brightness temperatures of individual clumps are in the range from $\sim 2 - 8$ K.

To show the general properties of the GMAs, we also measured the physical properties integrated over their size in Table 3. We define the area of the GMA by measuring the number of pixels above the threshold intensity of 5σ in the $^{12}\text{CO}(J=2-1)$ integrated intensity map. We calculated the “equivalent radius” if the measured areas are modeled as spherical clumps. The results are reported in Table 3 together with the resulting M_{H_2} integrated over the area. The derived values of M_{H_2} are therefore larger than that in Table 2, which only measured the mass within one synthesized beam at the intensity peak. The method to derive the M_{H_2} will be described in Sect. 3.2.2. Several factors are essential to consider for fair comparisons of our GMAs with other galaxies, such as beam size, filling factor, etc. A rough comparisons show that our GMAs in the starburst ring have physical extent of $\sim 200-300$ pc, which have similar order with the GMAs in other galaxies (e.g. Rand & Kulkarni 1990; Tosaki et al. 2007; Muraoka et al. 2009).

3.2.1. Spectra of the molecular clumps

We show in Figure 5 the spectra of the individual clumps selected above at their peak positions (i.e., within a synthesized beam). Most of the clumps show single gaussian profiles. The gaussian FWHM line widths of the clumps are determined by gaussian fitting, and are listed in Table 2.

The line widths we observed are quadratic sums of the intrinsic line widths and the galactic motion across the

synthesized beam, and the relation can be expressed as

$$\sigma_{\text{obs}}^2 = \sigma_{\text{rot}}^2 + \sigma_{\text{int}}^2, \quad (1)$$

where σ_{obs} is the observed FWHM line width, σ_{rot} is the line width due to the galactic rotation and the radial motions within the beam, and the σ_{int} is the intrinsic line width. The systematic galactic motion would be negligible if the spatial resolution is small enough. We subtract σ_{rot} as derived from a circular rotation model by fitting the rotation curve in Sect. 3.5. The derived intrinsic line width of the clumps are reported in Table 2. In general, there is $\sim 10-20\%$ difference between the observed and intrinsic line widths, which suggests that the galactic circular motions do not dominate the line broadening at this high resolution. However, the large “intrinsic” velocity dispersion thus derived by subtracting circular motions could still be dominated by non-circular motions, especially in the twin-peak region and in the dust lanes. We will mention this effect in the discussion.

In Table 2, we define the clumps based on their location and their velocity dispersions. The clumps in the ring are further designated by their velocity dispersion being broader or narrower than 30 km s^{-1} , and named respectively as B1,..., B3, and N1,..., N11, respectively. The clumps located at the dust lanes are named D1,..., D5.

3.2.2. Mass of the clumps

Radio interferometers have a discrete sampling of the uv coverage limited by both the shortest and longest baselines. Here, we estimate the effects due to the missing information. In Figure 6, we convolved our newly combined SMA data to match the beam size of the JCMT data ($21''$), and overlaid the spectra to compare the flux. The integrated $^{12}\text{CO}(J=2-1)$ fluxes of the JCMT and SMA data are $\sim 120 \text{ K km s}^{-1}$ and $\sim 71 \text{ K km s}^{-1}$, respectively. The integrated $^{13}\text{CO}(J=2-1)$ fluxes of the JCMT and SMA data are $\sim 15 \text{ K km s}^{-1}$ and $\sim 7 \text{ K km s}^{-1}$ respectively. Therefore our SMA data recover $\sim 60\%$ and $\sim 47\%$ of the $^{12}\text{CO}(J=2-1)$ and $^{13}\text{CO}(J=2-1)$ fluxes measured by the JCMT, respectively. If the missing flux is attributed to the extended emission, then the derived fluxes for the compact clumps will remain reliable. However, the spectra of the SMA data seem to have similar line profiles as that of the JCMT. Part of the inconsistency could then possibly be due to the uncertainty of the flux calibration, which are 15% and 20% for the JCMT and SMA, respectively. We note therefore that the following quantities measured from the flux will have uncertainties of at least 20% from the flux calibration.

There are several ways to calculate the molecular gas mass. The conventional H_2/I_{CO} (X_{CO}) conversion factor is one of the methods to derive the gas mass assuming that the molecular clouds are virialized. First, we use the ^{12}CO emission to calculate the molecular H_2 column density, N_{H_2} , as

$$N_{\text{H}_2} = X_{\text{CO}} \int T_{\text{b}} dv = X_{\text{CO}} I_{\text{CO}}, \quad (2)$$

where N_{H_2} for each clump is calculated by adopting the X_{CO} conversion factor of $3 \times 10^{20} \text{ cm}^{-2} (\text{K km s}^{-1})^{-1}$ (Solomon et al. 1987), T_{b} is the brightness temperature,

and dv is the line width. The values are listed in Table 2. Note that the X_{CO} has wide range of $0.5\text{--}4 \times 10^{20} \text{ cm}^{-2} (\text{K km s}^{-1})^{-1}$ (Young & Scoville 1991; Strong & Mattox 1996; Dame et al. 2001; Draine et al. 2007; Meier & Turner 2001; Meier et al. 2008). We adopted $3 \times 10^{20} \text{ cm}^{-2} (\text{K km s}^{-1})^{-1}$ to be consistent with Paper I. The surface molecular gas mass density Σ_{H_2} and the molecular gas mass M_{H_2} are thus calculated as,

$$\Sigma_{\text{H}_2} = N_{\text{H}_2} m_{\text{H}_2}, \quad (3)$$

$$M_{\text{H}_2} = \Sigma_{\text{H}_2} d\Omega, \quad (4)$$

where m_{H_2} and $d\Omega$ are the mass of a hydrogen molecule and the solid angle of the integrated area, respectively. Since this conversion factor is used for the $^{12}\text{CO}(J = 1 - 0)$ emission, we assume the simplest case where the ratio of $^{12}\text{CO}(J = 2 - 1)/^{12}\text{CO}(J = 1 - 0)$ is unity. The H_2 mass of the clumps measured within one synthesized beam are listed in Table 2. We would get the molecular gas mass (M_{gas}) by multiplying the H_2 mass by the mean atomic weight of 1.36 of the He correction.

The $^{12}\text{CO}(J = 2 - 1)$ is usually optically thick and only traces the surface properties of the clouds. Optically thinner $^{13}\text{CO}(J = 2 - 1)$ would be a better estimator of the total column density. We therefore calculate the average M_{H_2} in the nucleus and the ring to compare the M_{H_2} derived from both $^{12}\text{CO}(J = 2 - 1)$ and $^{13}\text{CO}(J = 2 - 1)$ lines. In the case of $^{12}\text{CO}(J = 2 - 1)$, the average M_{H_2} of the ring is about $1.7 \times 10^7 M_{\odot}$ within one synthesized beam, and the corresponding value for the nucleus is $3.4 \times 10^7 M_{\odot}$. However, in Paper I we derived the intensity ratio of $^{12}\text{CO}(J = 2 - 1)/^{12}\text{CO}(J = 1 - 0)$ is ~ 2 for the nucleus in the lower resolution map. Therefore the M_{H_2} of the nucleus is possibly smaller than that derived above. The conventional Galactic X_{CO} of $3 \times 10^{20} \text{ cm}^{-2} (\text{K km s}^{-1})^{-1}$ is often suggested to be overestimated in the galactic center and the starburst environment by a factor of 2 to 5 (e.g., Maloney & Black 1988; Meier & Turner 2001). Therefore, our estimated M_{H_2} in the ring and the nucleus might be smaller at least by a factor of 2.

Assuming the $^{13}\text{CO}(J = 2 - 1)$ emission is optically thin, and the $^{13}\text{CO}/\text{H}_2$ abundance of 1×10^{-6} (Solomon et al. 1979). We calculate the M_{H_2} with excitation temperature (T_{ex}) of 20 K and 50 K in LTE condition. The M_{H_2} of the nucleus averaged over one synthesized beam are $(7.0 \pm 2.5) \times 10^6 M_{\odot}$ and $(1.3 \pm 0.4) \times 10^7 M_{\odot}$ for 20 K and 50 K, respectively. The M_{H_2} of the ring averaged over one synthesized beam are $(5.8 \pm 2.5) \times 10^6 M_{\odot}$ and $(1.1 \pm 0.4) \times 10^7 M_{\odot}$ for 20 K and 50 K, respectively. With the assumption of constant $^{13}\text{CO}/\text{H}_2$ abundance, if the T_{ex} is ≤ 20 K, then the conversion factor we adopted for the ^{12}CO line is overestimated by a factor of ~ 3 to 5. The overestimation is smaller (a factor of 2 to 3) if the gas is as warm as 50 K. We measured the $^{12}\text{CO}(J = 2 - 1)$ flux higher than 3σ to derive the total H_2 mass of the nucleus and the ring. The total flux of the nucleus and the ring are $490.2 \pm 59.3 \text{ Jy km s}^{-1}$ and $2902.2 \pm 476.8 \text{ Jy km s}^{-1}$, respectively. If we adopted the intensity ratios of $^{12}\text{CO}(J = 2 - 1)$ and $^{12}\text{CO}(J = 1 - 0)$ are 1.9 ± 0.2 and

1.3 ± 0.2 for the nucleus and the ring (Paper I), the M_{H_2} of the nucleus and the ring are $(1.6 \pm 0.3) \times 10^8 M_{\odot}$ and $(1.4 \pm 0.3) \times 10^9 M_{\odot}$, respectively. Thus the nucleus and the ring account for 10% and 90% of the M_{H_2} within the 2 kpc circumnuclear region, respectively.

We calculate the virial mass of individual clumps by

$$M_{\text{vir}} = \frac{2r\sigma_{\text{rms}}^2}{G}, \quad (5)$$

where r is the radius of the clump derived in Sect. 3.2, and σ_{rms} is the three dimensional intrinsic root mean square velocity dispersion, which is equal to $\sqrt{(3/8\ln 2)\sigma_{\text{int}}}$. Since we observe the σ_{int} in one dimension, we need to multiply the observed σ_{int}^2 by 3. The radius is adopted with the size of the clumps assuming that σ_{int} is isotropic. The results are shown in Table 3. Note that the virial mass is for GMAs not GMCs, and we assume that the GMAs are bounded structures. The ratio of the virial mass M_{vir} and M_{gas} are shown in Table 3. We found that the narrow line clumps have $M_{\text{vir}}/M_{\text{gas}}$ that are more or less about unity, but are larger than unity for the broad line and dust lane clumps.

We plot the general properties of the molecular gas mass of individual molecular clumps in Figure 7. In Figure 7a, the histogram of the gas mass integrated over their size seems to be a power law with a sharp drop at the low mass end. This is due to the sensitivity limit, since the corresponding 3σ mass limit is $\sim 27 \times 10^6 M_{\odot}$ for a clump with a diameter of $3''.3$ (the average of the clumps in Table 3). In Figure 7b, the FWHM intrinsic line widths have a weak correlation with gas mass in the ring. In Figure 8a, we show the azimuthal variation of Σ_{H_2} calculated at the emission peaks of the clumps integrated over one synthesized beam. If we assume that NGC 1097 has a trailing spiral, then the direction of rotation is clockwise from east (0°) to north (90°). The Σ_{H_2} in the orbit crowding region is roughly from 0° to 45° , and from 180° to 225° . Note that the dust lane clumps typically have Σ_{H_2} similar to the narrow line ring clumps, which are lower than the broad line ring clumps in the orbit crowding region. The average Σ_{H_2} of the narrow line ring and dust lane clumps is $\sim 1800 M_{\odot} \text{ pc}^{-2}$, and $\sim 2300 M_{\odot} \text{ pc}^{-2}$ for the broad line ring clumps. In Figure 8b, the velocity dispersion of clumps located at the orbit crowding region and the dust lane are larger than that of the narrow line ring clumps. The average velocity dispersion of the narrow line clumps is $\sim 50 \text{ km s}^{-1}$, and $\sim 90 \text{ km s}^{-1}$ for the broad line ring/dust lane clumps. Given the similar line brightnesses (Table 2) of the peaks, the increased Σ_{H_2} are probably the results of increased line widths as it is indicated in equation (2). On the other hand, since the N_{H_2} is proportional to the number density of gas and line-of-sight path (i.e., optical depth), the higher Σ_{H_2} of the broad line clumps may be due to either a larger number density, or a larger line-of-sight path. We will discuss these effects in the discussion.

3.3. Young star clusters

To check how the star formation properties are associated with the molecular clumps in the ring, we compare the 6-cm radio continuum, V-band, and Pa α images with the molecular gas images. The 6-cm radio continuum sources are selected from the intensity peaks

(Hummel et al. 1987) at an angular resolution of $2''.5$. The V-band clusters (< 13 mag) are selected from the HST F555W image (Barth et al. 1995). These V-band selected clusters have typical size of 2 pc ($0''.03$), and are suspected to be super star clusters by Barth et al. (1995). Pa α clusters are identified in our HST F187N image described in the Sect. 2. The Pa α clusters are identified by SExtractor with main parameters of detection threshold of 15σ (DETECT_THRESH) and minimum number of pixels above threshold of 1 (DETECT_MINAREA). The number of deblending sub-thresholds is 50 for DEBLEND_NTHRESH and 0.0005 for DEBLEND_MINCONT. The parameters were chosen by a wide range of verifying and visual inspection.

We used 6-cm radio continuum and V-band selected clusters for the phenomenological comparison with the molecular clumps. To get a high resolution and uniform sample of star formation rate (SFR), we use the Pa α clusters in the following analysis.

In the $^{12}\text{CO}(J = 2-1)$ integrated intensity map (Figure 1), the star clusters and radio continuum sources are located in the vicinity of molecular clumps within the synthesized beam. The distribution of the massive star clusters is uniform in the ring instead of showing clustering in certain regions. The star clusters do not coincide with most of the CO peaks. The spatial correlation seems to be better in the peak brightness temperature map in Figure 1. Furthermore, there are no detected star clusters and radio continuum sources in the dust lane clumps, namely, clumps D1, D2, D3, and D4.

We corrected the extinction of the Pa α emission by the intensity ratio of H α (CTIO 1.5 m archived image) and Pa α . The PSFs of H α and Pa α are $\sim 1''.0$ and $\sim 0''.3$, respectively, and an additional convolving Gaussian kernel has been applied to both H α and Pa α images to match the CO beam size. The observed intensity ratio of H α and Pa α , $(I_{\text{H}\alpha}/I_{\text{Pa}\alpha})_o$, and the predicted intensity ratio $(I_{\text{H}\alpha}/I_{\text{Pa}\alpha})_i$ are multiplied by the extinction as follows:

$$\left(\frac{I_{\text{H}\alpha}}{I_{\text{Pa}\alpha}}\right)_o = \left(\frac{I_{\text{H}\alpha}}{I_{\text{Pa}\alpha}}\right)_i \times 10^{-0.4E(B-V)(\kappa_{\text{H}\alpha} - \kappa_{\text{Pa}\alpha})}, \quad (6)$$

where $E(B-V)$ is the color excess, $\kappa_{\text{H}\alpha}$ and $\kappa_{\text{Pa}\alpha}$ are the extinction coefficients at the wavelength of H α and Pa α , respectively.

The predicted intensity ratio of 8.6 is derived in the case B recombination with temperature and electron density of 10000 K and 10^4 cm^{-3} , respectively (Osterbrock 1989). The extinction coefficient of H α and Pa α are adopted from Cardelli's extinction curve (Cardelli et al. 1989), with $\kappa_{\text{H}\alpha} = 2.535$ and $\kappa_{\text{Pa}\alpha} = 0.455$, respectively. We derive the color excess $E(B-V)$ using equation (6), and derive the extinction of Pa α using the following equation,

$$A_\lambda = \kappa_\lambda E(B-V), \quad (7)$$

where A_λ is the extinction at wavelength λ . We show the derived values for $A_{\text{Pa}\alpha}$ and A_V in Table 4, where κ_V is 3.1 at V-band. The average extinction of the clumps at the wavelength of $1.88 \mu\text{m}$ (redshifted Pa α wavelength) is about 0.6 mag, which is quite transparent as compared with the extinction at the H α line of ~ 4 mag. We calculate SFRs using the Pa α luminosity based on the equation in Calzetti et al. (2008) of

$$\text{SFR}(M_\odot \text{ yr}^{-1}) = 4.2 \times 10^{-41} L_{\text{Pa}\alpha}(\text{erg s}^{-1}). \quad (8)$$

The SFR surface density (Σ_{SFR}) is thus calculated within the size of the CO synthesized beam ($1''.5 \times 1''.0$). Note that SFR cannot be determined in the dust lane clumps since we do not detect significant star clusters in both Pa α and H α images. The low Σ_{SFR} in the broad line ring and dust lane clumps seems to be unlikely due to the extinction, since the extinction of the broad line ring clumps are similar to that of the narrow line ring clumps, and the Σ_{H_2} of the dust lane clumps are similar to that of the narrow line ring clumps. To compare the star formation activities with the properties of the molecular gas, we measured the Σ_{SFR} at the position of each clump (Table 4). We show the correlation of Σ_{SFR} and the Σ_{H_2} of the molecular clumps in Figure 9a. This plot shows very little correlation. In Figure 10, we overlay our data on the plot of Σ_{SFR} and Σ_{H_2} used in Kennicutt (1998) to compare the small and the large scale star formation. The average number follows the Kennicutt-Schmidt correlation closely. However, we have either lower Σ_{SFR} or higher Σ_{H_2} than the global values in Kennicutt (1998). This might be because our spatial resolution is smaller than for their data. Recent investigations have shown that the power scaling relationship of the spatially-resolved Schmidt-Kennicutt law remains valid in the sub-kpc scale (Bigiel et al. 2008), to ~ 200 pc in M51 (Liu et al. 2010b) and M33 (Verley et al. 2010; Bigiel et al. 2010), but becomes invalid at the scale of GMC/GMAs (Onodera et al. 2010) because the scaling is overcome by the large scatter. The absence of a correlation in our 100 pc study is thus not surprising because even if the Schmidt-Kennicutt law is still valid, the scatter is expected to as large as ~ 0.7 dex (Liu et al. 2010b), larger than the dynamical range of the gas density in Figure 9a. Other possibilities to explain the inconsistency are the uncertain conversion factor mentioned in Sect. 3.2.2. The conversion factor is likely to be overestimated in the galactic center and starburst region. Moreover, regarding to the Schmidt-Kennicutt law was derived from the global galaxies that might be dominated by disk GMCs, our nuclear ring might not follow the same relation for its particular physical conditions.

As for the distribution of Σ_{SFR} in the ring, we find that Σ_{SFR} is low in the broad line clumps in Figure 9b, but do not have an obvious systematic azimuthal variation as Σ_{H_2} or intrinsic line width in Figure 8. In general, Σ_{SFR} is higher in the northern ring than in the southern ring. This distribution, as an average quantity, shows no strong dependence on location within the ring.

3.4. Physical conditions

3.4.1. Intensity ratio of multi-J CO lines

We compare the intensity ratio of the different CO lines on the same spatial scales by restricting the data to the same uv -range from 7.3 k λ to 79.6 k λ for the $^{12}\text{CO}(J = 2-1)$, $^{13}\text{CO}(J = 2-1)$ and $^{12}\text{CO}(J = 3-2)$ lines. The matched beam size of all maps is $3''.25 \times 2''.55$. We corrected for the primary beam attenuation in the maps. We measured the line intensities of individual clumps in the uv -matched integrated intensity maps, and calculated the intensity ratios in Table 5. The uv -matched low resolution maps do have some beam smearing effects on the spectra. However, an examination of the line profiles and attempts to correct for line smearing did not affect

the derived line ratios to within the experimental errors.

We estimate the density and temperature of the clumps with the LVG analysis (Goldreich & Kwan 1974) in a one-zone model. The collision rates of CO are from Flower & Launay (1985) for temperatures from 10 to 250 K, and from McKee et al. (1982) for 500 to 2000 K. We assume ^{12}CO and ^{13}CO abundances with respect to H_2 of 5×10^{-5} and 1×10^{-6} , with the observed velocity gradient of $\sim 1 \text{ km s}^{-1} \text{ pc}^{-1}$ of the ring. We determined the velocity gradient in the Paper I by the PV diagram, and it is consistent in this paper. The average ratio of the narrow and broad line clumps are used. Clumps N4, B1, D1, D2, D4, D5 are excluded in the average ratio because of their large uncertainty in R_{13} . Therefore the average R_{32} and R_{13} of the narrow line clumps are 1.00 ± 0.02 and 9.90 ± 2.11 , respectively. The average R_{32} and R_{13} of the broad line clumps are 0.72 ± 0.01 and 9.55 ± 1.56 , respectively. With the constraint of the intensity ratios within the uncertainty, the estimated temperature and density of the narrow line clumps are $\geq 250 \text{ K}$ and $(4.5 \pm 3.5) \times 10^3 \text{ cm}^{-3}$. The broad line clumps have temperatures of $45 \pm 15 \text{ K}$ and density of $(8.5 \pm 1.5) \times 10^2 \text{ cm}^{-3}$. The predicted brightness temperature (T_b) is $\sim 100 \text{ K}$ for the narrow line clumps and $\sim 20 \text{ K}$ for the broad line clumps. However, it seems to be inconsistent with the high/low Σ_{H_2} and low/high number density in the broad/narrow line clumps if we assume a constant scale height for the clumps. The solution may be a smaller beam filling factor for the narrow line clumps.

In Figure 9c, the R_{32} values have a positive correlation with Σ_{SFR} . In Figure 9d, similar to Σ_{SFR} , R_{32} is slightly lower in the broad line ring clumps and does not show any systematic pattern in the azimuthal direction.

3.5. Kinematics

Figure 11a is the intensity weighted isovelocity map of $^{12}\text{CO}(J = 2-1)$. The gas motion in the ring appears to be dominated by circular motion, while it shows clear non-circular motions in the $^{12}\text{CO}(J = 1-0)$ map as indicated by the S-shape nearly parallel to the dust lanes. As we discussed in Paper I, the non-significant non-circular motion in the $^{12}\text{CO}(J = 2-1)$ maps is perhaps because the dust lanes are not as strongly detected in $^{12}\text{CO}(J = 2-1)$ line, along with the fact that they are closer to the edge of our primary beam, or the non-circular motion is not prominent at the high spatial resolution. The circumnuclear gas is in general in solid body rotation. The velocity gradient of the blueshifted part is slightly steeper than the redshifted part. We also show the intensity weighted velocity dispersion map in Figure 11b. As we mentioned above, the velocity dispersion is larger in the twin-peak region, and lower in the region away from the twin-peak region.

The dynamical center of NGC 1097 was derived by Kohno et al. (2003) in their low resolution $^{12}\text{CO}(J = 1-0)$ map. With our high resolution $^{12}\text{CO}(J = 2-1)$ map, we expect to determine the dynamical center more accurately. We use the AIPS task **GAL** to determine the dynamical center. In the task **GAL**, $^{12}\text{CO}(J = 2-1)$ intensity-weighted velocity map (Figure 11) is used to fit a rotation curve. The deduced kinematic parameters are summarized in Table 6. We use an exponential curve to fit the area within $7''$ in radius. The observed rotation curve

and the fitted model curve are shown in Figure 12. From the fitted parameters, we find that the offset ($\sim 0''.3$) of the dynamical center with respect to the position of the AGN is still within a fraction of the synthesized beam size. The derived V_{sys} has a difference of $\sim 5 \text{ km s}^{-1}$ between $^{12}\text{CO}(J = 1-0)$ and $^{12}\text{CO}(J = 2-1)$ data, which is less than the velocity resolution of the data. Upon examining the channel maps of the $^{12}\text{CO}(J = 2-1)$ data, we find that the peak of the nuclear emission is almost coincident with the position of the AGN with an offset of $0''.3$. We therefore conclude that the position offset in the integrated intensity map, as mentioned in Sect. 3.1, is due to the asymmetric intensity distribution.

4. DISCUSSIONS

4.1. Molecular ring of NGC 1097

4.1.1. Twin-Peak structure

In the low resolution CO maps (Paper I, Kohno et al. 2003), NGC 1097 shows bright CO twin-peak structure arising at the intersection of the starburst ring and the dust lanes. The $\geq 300 \text{ pc}$ resolution CO data show that the barred galaxies usually have a large amount of central concentration of molecular gas (Sakamoto et al. 1999). Kenney et al. (1992) found that in several barred galaxies which host circumnuclear rings (M101, NGC 3351, NGC 6951), the central concentrations of molecular gas were resolved into twin-peak structures when resolution of $\sim 200 \text{ pc}$ is attained. A pair of CO intensity concentrations are found in these cases, in the circumnuclear ring, at the intersection of the ring and the dust lane. Their orientation is almost perpendicular to the major stellar bar. The twin-peak structure can be attributed to the orbit crowding of inflowing gas stream lines. The gas flow changes from its original orbit (the so called x_1 orbit) when it encounters the shocks, which results in a large deflection angle and migrate to new orbit (the so called x_2 orbit). The gas then accumulates in the family of the x_2 orbits in the shape of a ring or nuclear spirals (Athanasoulas 1992a; Piner et al. 1995). Intense massive star formation would follow in the ring/nuclear spiral once the gas becomes dense enough to collapse (Elmegreen 1994).

In our 100 pc resolution CO map, the starburst molecular ring is resolved into individual GMAs. In the orbit crowding region, we resolve the twin-peak into broad line clumps associated with the curved dust lanes. The narrow line clumps are located away from the twin-peak and are associated with star formation. This kind of “spectroscopic components” were also shown in several twin-peak galaxies at the intersection of dust lanes and circumnuclear ring, such as NGC 1365 (Sakamoto et al. 2007), NGC 4151 (Dumas et al. 2010), NGC 6946 (Schinnerer et al. 2007), and NGC 6951 (Kohno et al. 1999). However, most of the spectra at these intersections show blended narrow/broad line components, which is perhaps due to insufficient angular resolution. Our observations for the first time spatially resolved these two components toward the twin-peak region of NGC 1097.

It is interesting to note that the circumnuclear ring is nearly circular at $\sim 42^\circ$ inclination, which indicates its intrinsic elliptical shape in the galactic plane. The schematic sketch is shown in Figure 14. The loci of

dust lanes are invoked to trace the galactic shock wave, and their shapes are dependent on the parameters of the barred potential. In the case of NGC 1097, the observed dust lanes resemble the theoretical studies (Athanasoulas 1992b), with a pair of straight lanes that slightly curve inwards in the inner ends. These findings are consistent with the predicted morphology from bar-driven nuclear inflow. The physical properties of these clumps are discussed in the following subsection.

4.1.2. The nature of the molecular clumps in the ring

In Figure 1 and Table 2, the peak brightness temperatures of individual clumps are from 2 to 8 K. These values are lower than the typical temperatures of molecular gas as expected in the environment of a starburst (~ 100 K), and as estimated by our LVG results in Paper I and this work. This lower brightness temperature may be due to the small beam filling factor:

$$f_b = \left(\frac{\theta_s^2}{\theta_s^2 + \theta_b^2} \right) \sim \left(\frac{\theta_s^2}{\theta_b^2} \right), \quad (9)$$

$$f_b = \left(\frac{T_b}{T_c} \right) \quad (10)$$

where f_b is the beam filling factor, θ_s and θ_b are the source size and the beam size, respectively. We assume $\theta_s \ll \theta_b$. T_b is the brightness temperature and T_c is the actual temperature of the clouds. We assume here that the source size is compact and much smaller than the beam. If we assume the LVG predicted $T_b \sim 100$ K Sect. 3.4.1 for narrow line ring clumps, and an average observed $T_b \sim 5$ K, then $f_b \sim 0.05$. This suggests θ_s is ~ 20 pc or association of much smaller clumps for the narrow line ring clumps. In the case of the broad line ring clumps, with an average observed T_b of ~ 5 K and LVG predicted T_b of ~ 20 K, then f_b is ~ 0.25 and $\theta_s \sim 44$ pc. The size of the broad line ring clumps is a factor of 2 higher than the narrow line ring clumps. Given the estimated low volume number density of the broad line clumps in Sect. 3.4.1, the inconsistency between high Σ_{H_2} and low number density mentioned is possibly due to the large line-of-sight path, or larger scale height of the broad line clumps. If the assumption of a spherical shape of the clumps hold, the larger size estimated above seems to be consistent with this scenario. However, considering the higher opacity of the broad line clumps as suggested by the high Σ_{H_2} , it is likely that we are tracing the diffuse and cold gas at the surface of GMA rather than the dense and warm gas. On the other hand, the narrow line clumps show the opposite trends to trace the relatively warm and dense gas.

4.1.3. Azimuthal variation of the line widths and Σ_{H_2}

In Figure 8, we found the observed (and intrinsic) line widths, and Σ_{H_2} , show variations along the azimuthal direction in the ring. There are local maxima of line widths and Σ_{H_2} at the position of the twin-peak at the orbit crowding regions. Since the brightness temperature does not vary dramatically between the emission peaks along the ring, the deduced peaks in H_2 column density can be directly attributed to the increased line widths. Beam smearing is possibly important as multiple streams may converge within a synthesized beam.

However, as shown in Fig 11b, enhanced line widths occur even over extended regions. The intrinsic velocity dispersion of both the narrow and the broad line clumps cannot be thermal, as the implied temperature would be 2000–10000 K. In the Galactic GMCs, non-thermal line broadening has been attributed to turbulence from unknown mechanisms. In the case of NGC 1097, turbulence could have been generated by shocks of the orbit crowding region. Shocked gas as indicated by H_2 S(1-0) emission has been reported toward the twin-peak of NGC 1097 (Kotilainen et al. 2000). The narrow line clumps further along the ring may be due to subsequent dissipation of the kinetic energy from the shock wave. This kind of large velocity widths up to ~ 100 km s $^{-1}$ were also observed in NGC 6946. With resolutions down to GMC-scale of 10 pc, multiple components in the spectra were seen at the nuclear twin-peak by Schinnerer et al. (2007). However, the mechanism to cause the broadened line widths is not clear at this scale.

As noted earlier, the “intrinsic” line widths we derived contain not only the random dispersion but also the velocity gradients due to non-circular motions generated by shock fronts. However, our observations do not have sufficient angular resolution to resolve the locations and magnitudes of the discrete velocity jumps to be expected across the shock front (Draine & McKee 1993). A detailed hydrodynamical model is also needed to quantitatively predict the magnitude of the non-circular velocity gradient in the ring.

4.2. Gravitational stabilities of the GMAs in the starburst ring

How do the GMAs form in the starburst ring? In the ring of NGC 1097, we consider gravitational collapse due to Toomre instability (Toomre 1964). We estimate the Toomre Q parameter ($\Sigma_{\text{crit}}/\Sigma_{\text{gas}}$) to see if the rotation of the ring is able to stabilize against the fragmentation into clumps. Here the Toomre critical density can be expressed as:

$$\Sigma_{\text{crit}} = \alpha \left(\frac{\kappa \sigma_{\text{int}}}{3.36G} \right), \quad (11)$$

$$\kappa = 1.414 \left(\frac{V}{R} \right) \left(1 + \frac{R}{V} \frac{dV}{dR} \right)^{0.5}, \quad (12)$$

where the constant α is unity, G is the gravitational constant, κ is the epicycle frequency, V is rotational velocity, and R is the radius of the ring. If Σ_{H_2} exceeds Σ_{crit} , then the gas will be gravitationally unstable and collapse. We approximate the velocity gradient dV/dR as close to zero in Figure 12. because of the flat rotation curve of the galaxy at the position of the starburst ring. Therefore $\kappa \sim 1.414V/R$. V is ~ 338 km s $^{-1}$ in the galactic plane assuming an inclination of $\sim 42^\circ$. We find the ratio of $\Sigma_{\text{crit}}/\Sigma_{H_2}$ is less than unity in the ring (~ 0.6). Since Σ_{gas} consists of H_2 , HI, and metals, this ratio of 0.6 is an upper limit. However, the HI is often absent in centers of galaxies, and NGC 1097 also shows a HI hole in the central 1' (Higdon & Wallin 2003). Hence the HI gas does not have an important contribution in the nuclear region. A ratio less than unity suggests that the ring is unstable and will fragment into clumps.

As for whether the GMA itself is gravitational bound or not, in Sect. 3.2.2 we found that $M_{\text{vir}}/M_{\text{gas}}$ is around unity in the narrow line clumps and larger than unity by a factor of more than 2 in the broad line clumps. This seems to suggest that the broad line clumps are not virialized, probably because of the larger turbulence. However, there are several factors to reduce the ratio. First, since we do not subtract the non-circular motion in the broad line clumps, the observed $M_{\text{vir}}/M_{\text{gas}}$ should be an upper limit. We can estimate how large the non-circular motion is if we assume the $M_{\text{vir}}/M_{\text{gas}}$ of the broad line clumps is unity. The magnitude of the non-circular motion is from 50 to 100 km s $^{-1}$ for the broad line clumps under this assumption. Athanassoula (1992a) showed that there is a correlation between the bar axial ratio and the velocity gradient (jump) across the shock wave. NGC 1097 has a bar axial ratio of ~ 2.6 (Menéndez-Delmestre et al. 2007), which indicates the maximum velocity jump is ~ 70 km s $^{-1}$ (Figure 12; Athanassoula 1992b). However, this number is supposed to be an upper limit since it was measured at the strongest strength of the shock, where the strength of the shock is a function of position relative to the nucleus. The shock strength seems to be weaker at the intersection of the circumnuclear ring than for the outer straight dust lanes, as suggested in the model. Hence we expect the velocity gradient caused by shock front is smaller than ~ 70 km s $^{-1}$, based on this correlation. In this case, the broad line clumps still have 20% larger velocity dispersion than narrow line clumps. Second, the size of the clumps will also be a possible factor to reduce the $M_{\text{vir}}/M_{\text{gas}}$ to unity. In Sect. 4.1.2, we estimate that the filling factor of the broad line clumps is ~ 0.25 , and therefore the intrinsic radius will be smaller by a factor of $0.25^{1/2} \sim 0.5$. Third, in Sect. 3.2.2, we point out the molecular gas mass derived from $^{12}\text{CO}(J = 2-1)$ might be underestimated at least by a factor of ~ 2 . These factors also can lower the $M_{\text{vir}}/M_{\text{gas}}$ to roughly unity in most of the broad line clumps and hence the GMA could also be gravitationally bound in the broad line clumps.

4.3. Star formation in the ring

4.3.1. Extinction

The distribution of the massive star clusters is uniform in the ring instead of highly clustering in certain clumps in Figure 1. The star clusters do not coincide with most of the CO peaks. This could be due to several reasons such as extinction or the physical nature of the star clusters. Of course, since we are comparing the scale of star clusters (2 pc) with that of GMAs (100 pc), we are not able to conclude the physical correlation by their spatial distribution. The Pa α is more transparent than the commonly used H α through dust extinction. However, the foreground extinction ($E(B-V) \sim 1.3$) for the Pa α clusters corresponds to a hydrogen column density of 6.4×10^{21} cm $^{-2}$ (Diplas & Savage 1994) averaged over one synthesized beam. This is much less than the average H $_2$ column density for the molecular clumps in the ring, which is $\sim 8.7 \times 10^{22}$ cm $^{-2}$. Therefore, this suggests that the detected Pa α clusters might be located on the surface of the clouds instead of being embedded inside the clumps, or else located away from the clouds. However, it can not be ruled out that there are deeply embedded

stellar clusters in the CO peaks in this scenario.

There is also a deficiency of star clusters in the broad line clumps associated with the dust lanes. This again could be due to extinction although we found it is similar in the star forming ring and the dust lanes. However, it is interesting that there is a spatial offset between the Spitzer 24 μm peaks and the CO peaks, and the FIR emission in the dust lane is intrinsically faint based on Herschel PACS 70 and 100 μm maps (Sandstrom et al. 2010). The long wavelength IR maps are less affected by extinction, and suggest a lack of newly formed star clusters in the dust lanes. However, a higher resolution for the FIR observation is needed to confirm the star formation activities in the broad line clumps.

4.3.2. Molecular gas and star formation

In NGC 1097, the mechanisms of the intensive star formation in the ring are still uncertain. It could be induced by the gravitational collapse in the ring stochastically (Elmegreen 1994). The other possible mechanism is that the stars form in the downstream of the dust lane at the conjunction of the ring, and the star clusters continue to orbit along the ring (e.g., Böker et al. 2008). The major difference is that the latter scenario will have an age gradient for the star clusters along the ring while it is randomized in the previous case. Several papers have discussed these mechanisms in the galaxies that have star forming rings and there is no clear answer so far (e.g., Mazzuca et al. 2008; Böker et al. 2008; Buta et al. 2000). Sandstrom et al. (2010) tested the above pictures by examining if there is an azimuthal gradient of dust temperature in the ring of NGC 1097, assuming that the younger population of massive star clusters will heat the dust to higher temperatures than older clusters. There seems to be no gradient, though it is difficult to conclude since a few rounds of galactic rotation might smooth out the age gradient. We do not aim to solve the above question in this paper since the most direct way is to measure the age of the star clusters, and this needs detailed modeling. It is interesting to compare the properties of the molecular clumps with star clusters since the molecular clouds are the parent site of star formation. The one relevant result here is that the line widths are narrower further away from where the molecular arms join the ring. This could be related to the dissipation of turbulence which may allow cloud collapse to proceed.

In Figure 9(b), we found that Σ_{SFR} , compared with velocity dispersion (Figure 8), has no significant azimuthal correlation. Furthermore, R_{32} shows a similar trend to Σ_{SFR} as a function of azimuthal direction (Figure 9(d)), where R_{32} and Σ_{SFR} has a correlation in Figure 9(c). This suggests that Σ_{SFR} and R_{32} are physically related, but might not be associated with the large scale dynamics in this galaxy. Although Σ_{SFR} seems to be suppressed in the broad line clumps. Nevertheless, in Figure 9(b)&(d) we consider that the standard deviations of the measured Σ_{SFR} do not significantly diverse among global variations. The standard deviations are $0.7 \text{ M}_{\odot} \text{ yr}^{-1} \text{ kpc}^{-2}$ and $0.4 \text{ M}_{\odot} \text{ yr}^{-1} \text{ kpc}^{-2}$ of the northeast and southwest of the ring, respectively. The mean values of the Σ_{SFR} are $3.3 \text{ M}_{\odot} \text{ yr}^{-1} \text{ kpc}^{-2}$ and $1.4 \text{ M}_{\odot} \text{ yr}^{-1} \text{ kpc}^{-2}$ of the northeast and southwest of the ring, respectively. With the limited points, our results suggest that the star formation activities are randomly generated on the local

scale instead of a systematic distribution.

In Figure 13, we show how the R_{32} ratio varies for different densities and kinetic temperatures. It shows that when R_{32} varies from 0.3 to 0.9, the required number density of molecular gas changes from 10^2 cm^{-3} to $5 \times 10^3 \text{ cm}^{-3}$. The R_{32} seems to be dependent on the density more than the temperature when it is below unity. Hence the variation of R_{32} indicates different density among clumps. It is interesting to note that there is a correlation between R_{32} and SFR, and some clumps (N1, N2, N7) which have higher SFR values are spatially close to the HCN($J = 1-0$) peaks (Kohno et al. 2003). Higher values of R_{32} will select denser gas associated with higher SFR, as has been shown in the large scale observations of HCN and FIR correlation (Gao, Solomon, & Philip 2004). In the smaller GMC-scale, Lada (1992) also showed that the efficiency of star formation is higher in the dense core rather than in the diffuse gas. The ratio map of R_{32} can be useful to determine the location of star formation.

5. SUMMARY

1. We show the multi-J CO line maps of NGC 1097 toward the 1 kpc circumnuclear region. The molecular ring is resolved into individual GMAs in the star forming ring, the dust lanes, and at the twin-peak structures. For the first time the molecular concentration at the twin-peak is resolved in to two populations of GMAs in terms of velocity dispersion and physical conditions. The clumps in the starburst ring have narrower velocity dispersion while the line widths are broader in the dust lanes, and for some clumps located in the twin-peak. The physical and kinematic properties are different for these clumps. The narrow line clumps have higher temperature ($\geq 250 \text{ K}$) and density ($(4.5 \pm 3.5) \times 10^3 \text{ cm}^{-3}$) in contrast to the broad line clumps ($T = 45 \pm 15 \text{ K}$; $N_{\text{H}_2} = (8.5 \pm 1.5) \times 10^2 \text{ cm}^{-3}$ based on the LVG analysis).
2. The Toomre-Q factor is smaller than unity in the molecular ring suggesting that the GMAs could form via gravitational instability in the ring, where the Σ_{H_2} of the clumps is large enough to overcome the critical density. The narrow line clumps are gravitationally bound as shown by the values of $M_{\text{vir}}/M_{\text{gas}}$ which are nearly unity. Although $M_{\text{vir}}/M_{\text{gas}}$ is larger than unity in the broad line clumps, by accounting for non-circular motions, smaller intrinsic source sizes, and the underestimation of molecular gas mass, we can lower $M_{\text{vir}}/M_{\text{gas}}$ to unity. Therefore both systems are likely to be gravitationally bound.
3. The SFR is correlated to R_{32} , suggesting that the star formation activities and the physical conditions of the molecular gas are associated with each other. In contrast to the velocity dispersion and the Σ_{H_2} , the SFR and R_{32} are not correlated with the large scale dynamics. This suggests that the visible star formation activities remain a localized phenomenon. The SFR is lower in the broad line clumps than in the narrow line clumps, which may be intrinsically suppressed in the dust lanes.

We thank the SMA staff for maintaining the operation of the array. We appreciate for referee's detail comments to improve the manuscript. We thank G. Petitpas for providing the JCMT data. P.-Y. Hsieh especially acknowledges the fruitful discussions with L.-H. Lin, K. Sakamoto, N. Scoville, W. Maciejewski, and L. Ho for the manuscript. This project is funded by NSC 97-2112-M-001-007-MY3 and NSC 97-2112-M-001-021-MY3.

Facilities: SMA, HST (NICMOS)

Table 1
SMA observation parameters

	230 GHz	230 GHz	230 GHz	345 GHz
Parameters	Compact-N	Extended	Very extended	Compact
Date	2004-07-23, 2004-10-01	2005-09-25	2005-11-07	2006-09-05
Phase center (J2000.0):				
R.A.		$\alpha_{2000} = 02^{\text{h}}46^{\text{m}}18^{\text{s}}.96$		
Decl.		$\delta_{2000} = -30^{\circ}16'28''897$		
Primary beams		52''		36''
No. of antennas	8, 8	6	7	7
Project baseline range (k λ)	5 – 74, 10 – 84	23 – 121	12 – 390	7.2 – 80
Bandwidth (GHz)			1.989	
Spectral resolution (MHz)	0.8125, 3.25	0.8125	0.8125	0.8125
Central frequency, LSB/USB (GHz)		219/228		334/344
τ_{225}^{b}	0.15, 0.3	0.06	0.1	0.06
$T_{\text{sys,DSB}}$ (K)	200, 350	110	180	300
Bandpass calibrators	Uranus, J0423 – 013	3C454.3	3C454.3, 3C111	Uranus, Neptune
Absolute flux calibrators ^a	Uranus (36.8, 34.2), J0423 – 013 (2.8, 2.5)	Uranus (37.2), 3C454.3 (21.3)	Uranus (34.9), 3C454.3 (21.3)	Neptune (21.1)
Gain calibrators	J0132 – 169	J0132 – 169	J0132 – 169	J0132 – 169, J0423 – 013

^a The numbers in the parenthesis are the absolute flux in Jy.

^b τ_{225} is the optical depth measured in 225 GHz.

Table 2
Physical parameters of the peaks of the molecular clouds

ID	δ R.A. (1) (")	δ Decl. (2) (")	I_{CO} (3) (Jy beam $^{-1}$ km s $^{-1}$)	δV_{obs} (4) (km s $^{-1}$)	δV_{int} (5) (km s $^{-1}$)	N_{H_2} (6) (10^{22} cm $^{-2}$)	Σ_{H_2} (7) (M_{\odot} pc $^{-2}$)	M_{H_2} (8) (10^6 M_{\odot})	T_{b} (9) (K)
N1	9.0	1.6	17.2	54 \pm 3	42 \pm 4	7.9	1270	10.7	4.1
N2	8.6	4.8	27.9	67 \pm 3	61 \pm 4	12.8	2070	17.3	5.5
N3	3.6	8.4	38.3	69 \pm 1	64 \pm 1	17.6	2840	23.8	7.5
N4	0.6	8.2	18.5	62 \pm 4	56 \pm 4	8.5	1370	11.5	5.8
N5	-4.8	7.8	21.3	38 \pm 1	31 \pm 1	9.8	1580	13.2	6.1
N6	-6.4	5.6	19.6	41 \pm 2	37 \pm 2	9.0	1460	12.2	4.1
N7	-8.6	-2.6	40.3	61 \pm 2	52 \pm 3	18.5	2990	25.0	8.0
N8	-5.4	-8.4	28.4	57 \pm 2	51 \pm 2	13.1	2110	17.6	5.8
N9	-2.8	-9.2	24.6	62 \pm 3	57 \pm 3	11.3	1820	15.2	4.1
N10	4.8	-7.8	19.7	43 \pm 2	37 \pm 2	9.1	1460	12.2	6.1
N11	7.8	-6.6	27.7	52 \pm 4	49 \pm 4	12.7	2050	17.2	5.8
B1	10.2	3.6	27.8	113 \pm 10	109 \pm 11	12.7	2060	17.2	2.4
B2	-7.4	-6.8	34.8	99 \pm 5	96 \pm 5	16.0	2580	21.6	4.6
B3	-5.4	-6.6	31.3	94 \pm 8	90 \pm 8	14.4	2320	19.4	4.1
D1	16.8	-1.4	18.9	100 \pm 10	97 \pm 10	8.7	1400	11.7	1.8
D2	12.8	1.6	21.1	86 \pm 17	82 \pm 18	9.7	1560	13.1	2.0
D3	-17.8	2.6	16.2	81 \pm 7	78 \pm 8	7.5	1200	10.1	1.8
D4	-13.0	-1.0	24.4	84 \pm 5	80 \pm 6	11.2	1810	15.1	3.5
D5	-10.0	-4.0	38.6	118 \pm 4	115 \pm 4	17.7	2860	24.0	4.6
Nu	0	0	50.4	52 \pm 5	-	16.1	3740	23.2	-
Nu	0	0	-	57 \pm 5	-	-	-	-	-
Nu	0	0	-	186 \pm 20	-	-	-	-	-

Note. — We define the peaks based on their location and their velocity dispersions. The clumps in the dust lanes (molecular spiral arms) are named D1, ..., D5. The clumps in the ring are further designated by their velocity dispersion being broader or narrower than 30 km s $^{-1}$, and named respectively as B1, ..., B3, and N1, ..., N11. Nu is the ID of the nucleus. (1) R.A. offsets from the phase center. (2) Dec. offsets from the phase center. (3) Integrated CO(J = 2 – 1) intensity. The uncertainty is 2.2 Jy beam $^{-1}$ km s $^{-1}$. (4) Fitted FWHM for the observed line width. The nucleus has multiple-gaussians profile, and we list the fitted line widths with 3 gaussians. Note that the I_{CO} , N_{H_2} , and Σ_{H_2} of the nucleus is the sum value of the three components. (5) FWHM line width of intrinsic velocity dispersion. (6) H $_2$ column density with the uncertainty of 1.1×10^{22} cm $^{-2}$. (7) Σ_{H_2} with the uncertainty of 170 M_{\odot} pc $^{-2}$. (8) Mass of molecular H $_2$ within the synthesized beam ($1''.5 \times 1''.0$). The uncertainty is $1.4 \times 10^6 \text{ M}_{\odot}$. (9) Peak brightness temperature.

Table 3
Physical parameters of the GMAs

ID	Diameter (1) ($''$)	M_{H_2} (2) ($10^6 M_\odot$)	M_{gas} (3) ($10^6 M_\odot$)	M_{vir} (4) ($10^6 M_\odot$)	$M_{\text{vir}}/M_{\text{gas}}$ (5)
N1	2.9	32.4 ± 5.3	44.1 ± 7.2	44.9 ± 10.2	1.0 ± 0.3
N2	3.7	71.2 ± 8.7	96.9 ± 11.8	118.0 ± 16.3	1.2 ± 0.2
N3	3.5	73.6 ± 7.9	100.1 ± 10.8	125.4 ± 5.9	1.3 ± 0.1
N4	2.2	17.7 ± 3.0	24.0 ± 4.1	58.6 ± 9.6	2.4 ± 0.6
N5	2.9	37.5 ± 5.5	51.0 ± 7.4	25.1 ± 2.7	0.5 ± 0.1
N6	2.9	33.8 ± 5.6	46.0 ± 7.6	34.6 ± 5.2	0.8 ± 0.2
N7	3.4	79.1 ± 7.6	107.5 ± 10.3	79.3 ± 9.9	0.7 ± 0.1
N8	2.5	51.5 ± 4.2	70.0 ± 5.7	57.5 ± 5.6	0.8 ± 0.1
N9	3.7	94.5 ± 8.8	128.5 ± 12.0	104.2 ± 14.1	0.8 ± 0.1
N10	2.8	32.7 ± 5.2	44.5 ± 7.1	34.3 ± 4.1	0.8 ± 0.2
N11	4.1	133.1 ± 11.1	181.0 ± 15.0	85.8 ± 15.1	0.5 ± 0.1
B1	3.1	48.6 ± 6.3	66.1 ± 8.6	316.6 ± 71.0	4.8 ± 1.2
B2	3.3	80.0 ± 7.2	108.8 ± 9.9	267.4 ± 29.8	2.5 ± 0.4
B3	3.0	77.0 ± 5.7	104.7 ± 7.7	208.8 ± 43.4	2.0 ± 0.4
D1	3.3	56.5 ± 6.9	76.9 ± 9.4	269.1 ± 62.8	3.5 ± 0.9
D2	3.5	58.6 ± 8.2	79.7 ± 11.1	207.7 ± 102.0	2.6 ± 1.3
D3	2.9	30.1 ± 5.5	41.0 ± 7.4	152.3 ± 34.2	3.7 ± 1.1
D4	5.4	117.7 ± 18.9	160.0 ± 25.7	303.0 ± 47.2	1.9 ± 0.4
D5	4.1	112.6 ± 11.0	153.1 ± 15.0	474.8 ± 36.8	3.1 ± 0.4

Note. — (1) Diameter of the clumps. (2) H_2 mass integrated over the diameter of the clumps. (3) Gas mass integrated over the diameter of the clumps. The M_{gas} is the M_{H_2} corrected with the He fraction of 1.36 in Sect.refsect-mass. (4) Virial mass of the clumps. (5) Ratio of the virial mass to the M_{gas} . We have not corrected for the beam convolution effect as the derived diameters are sufficiently large. We think the assumption of Gaussian shapes may be the greater source of error.

Table 4
Star formation properties

ID	$F_{\text{Pa}\alpha}$ (1) ($10^{-14} \text{ erg s}^{-1} \text{ cm}^{-2}$)	$E(\text{B-V})$ (2) (mag)	$A_{\text{Pa}\alpha}$ (3) (mag)	A_{V} (4) (mag)	Σ_{SFR} (5) ($\text{M}_{\odot} \text{ yr}^{-1} \text{ kpc}^{-2}$)
N1	6.03 ± 0.55	1.41 ± 0.01	0.64 ± 0.30	4.36 ± 0.04	2.74 ± 0.25
N2	7.01 ± 0.39	1.06 ± 0.01	0.48 ± 0.23	3.30 ± 0.04	3.18 ± 0.18
N3	4.00 ± 0.22	1.02 ± 0.02	0.46 ± 0.22	3.16 ± 0.06	1.81 ± 0.10
N4	8.95 ± 0.62	1.21 ± 0.01	0.55 ± 0.26	3.75 ± 0.03	4.06 ± 0.28
N5	7.52 ± 0.38	1.00 ± 0.01	0.46 ± 0.22	3.11 ± 0.03	3.41 ± 0.17
N6	7.94 ± 0.37	0.97 ± 0.01	0.44 ± 0.21	3.00 ± 0.03	3.60 ± 0.17
N7	8.97 ± 0.75	1.36 ± 0.01	0.62 ± 0.29	4.20 ± 0.03	4.07 ± 0.34
N8	4.21 ± 0.41	1.45 ± 0.02	0.66 ± 0.31	4.50 ± 0.06	1.91 ± 0.19
N9	3.72 ± 0.35	1.41 ± 0.02	0.64 ± 0.30	4.36 ± 0.07	1.69 ± 0.16
N10	2.90 ± 0.30	1.47 ± 0.03	0.67 ± 0.32	4.56 ± 0.09	1.32 ± 0.14
N11	1.92 ± 0.22	1.49 ± 0.05	0.68 ± 0.32	4.62 ± 0.14	0.87 ± 0.10
B1	2.55 ± 0.19	1.17 ± 0.03	0.53 ± 0.25	3.62 ± 0.10	1.16 ± 0.09
B2	2.60 ± 0.24	1.35 ± 0.03	0.61 ± 0.29	4.18 ± 0.10	1.18 ± 0.11
B3	1.29 ± 0.17	1.44 ± 0.07	0.65 ± 0.31	4.45 ± 0.21	0.58 ± 0.08
D1	≤ 0.12	-	-	-	-
D2	≤ 0.12	-	-	-	-
D3	≤ 0.12	-	-	-	-
D4	≤ 0.12	-	-	-	-
D5	1.56 ± 0.16	1.31 ± 0.05	0.60 ± 0.28	4.07 ± 0.17	0.71 ± 0.07

Note. — (1) Pa α flux corrected by the extinction measured in the CO clumps. The upper limit of the clumps (D1, ..., D4) is $1.21 \times 10^{-15} \text{ erg s}^{-1} \text{ cm}^{-2}$. (2) Color excess. (3) Extinction at wavelength of Pa α in the unit of magnitude. (4) Extinction at V-band in the unit of magnitude. (5) Surface density of SFR. The upper limit is $0.05 \text{ M}_{\odot} \text{ yr}^{-1} \text{ kpc}^{-2}$.

Table 5
Intensity ratios of the CO clumps

ID	R_{32} (1)	R_{13} (2)
N1	1.18 ± 0.07 (0.78 ± 0.18)	10.52 ± 7.05
N2	0.89 ± 0.03 (1.02 ± 0.14)	9.17 ± 2.92
N3	1.22 ± 0.04	8.12 ± 2.35
N4	1.41 ± 0.09	-
N5	1.68 ± 0.09	12.44 ± 9.74
N6	1.19 ± 0.07	12.47 ± 9.50
N7	0.92 ± 0.02 (0.99 ± 0.06)	8.52 ± 1.71
N8	0.62 ± 0.02 (0.50 ± 0.06)	10.24 ± 3.17
N9	0.66 ± 0.03	10.88 ± 5.14
N10	0.85 ± 0.05	7.18 ± 2.73
N11	0.78 ± 0.03	13.04 ± 6.45
B1	0.79 ± 0.03	-
B2	0.71 ± 0.02	6.51 ± 1.10
B3	0.72 ± 0.02	11.49 ± 3.74
D1	0.76 ± 0.08	-
D2	0.86 ± 0.05	-
D3	1.19 ± 0.12	-
D4	0.72 ± 0.03	-
D5	0.72 ± 0.02 (0.39 ± 0.03)	10.65 ± 2.59 (8.38 ± 3.41)
Nu	0.93 ± 0.02	23.37 ± 9.79

Note. — (1) $^{12}\text{CO}(J = 3-2)/(J = 2-1)$ intensity ratios derived from CO brightness temperature. Numbers within parenthesis are beam smearing corrected ratios. (2) $^{12}\text{CO}(J = 2-1)/^{13}\text{CO}(J = 2-1)$ intensity ratios derived from CO brightness temperature. Numbers within parenthesis are beam smearing corrected ratios. All the quantities are measured with a beam size of $3''.25 \times 2''.55$.

Table 6
Dynamical parameters fitted by GAL

Parameters	Value
R.A.	$02^{\text{h}}46^{\text{m}}18^{\text{s}}.95$
Decl.	$-30^{\circ}16'29''.13$
Position angle	$133^{\circ}0 \pm 0^{\circ}.1$
Inclination	$41^{\circ}7 \pm 0^{\circ}.6$
Systemetic velocity (km s^{-1} ; V_{sys})	1249.0 ± 0.5
V_{max} (km s^{-1})	387.6 ± 4.3
R_{max}	$9''.5 \pm 0''.1$

Note. — The 6-cm peak of the nucleus is R.A. = $02^{\text{h}}46^{\text{m}}18^{\text{s}}.96$, Decl. = $-30^{\circ}16'28''.897$.

REFERENCES

- Aalto, S., Booth, R. S., Black, J. H. & Johansson, L. E. B. 1995, *A&A*, 300, 369
- Athanassoula, E. 1992a, *MNRAS*, 259, 328
- Athanassoula, E. 1992b, *MNRAS*, 259, 345
- Barth, A. J., Ho, L. C., Filippenko, A. V., & Sargent, W. L. 1995, *AJ*, 110, 1009
- Böker, T., Falcón-Barroso, J., Schinnerer, E., Knapen, J. H., & Ryder, S. 2008, *AJ*, 135, 479
- Bigiel, F., Leroy, A., Walter, F., Brinks, E., de Blok, W. J. G., Madore, B., & Thornley, M. D. 2008, *AJ*, 136, 2846
- Bigiel, F., Bolatto, A. D., Leroy, A. K., Blitz, L., Walter, F., Rosolowsky, E. W., Lopez, L. A., & Plambeck, R. L. 2010, *ApJ*, 725, 1159
- Buta, R., Treuthardt, P. M., Byrd, G. G., & Crocker, D. A. 2000, *AJ*, 120, 1289
- Cardelli, J. A., Clayton, G. C., & Mathis, J. S. 1989, *ApJ*, 345, 245
- Calzetti, D. 2007, *NCimB*, 122, 971
- Clark, B. G. 1980, *A&A*, 89, 377
- Combes, F. & Gerin, M. 1985, *A&A*, 150, 327
- Dame, T. M., Hartmann, Dap & Thaddeus, P. 2001, *ApJ*, 547, 792
- Davies, R. I., Maciejewski, W., Hicks, E. K. S., Tacconi, L. J., Genzel, R. & Engel, H. 2009 *ApJ*, 702, 114
- Diplas, A., & Savage, B. D. 1994, *ApJ*, 427, 274
- Draine, B. T., McKee, C. F. 1993, *ARA&A*, 31, 373
- de Vaucouleurs, G., de Vaucouleurs, A., Corwin, H. G., Jr., Buta, R. J., Paturel, G., & Fouqué, P. 1991, *Third Reference Catalogue of Bright Galaxies* (New York: Springer-Verlag)
- Draine, B. T. et al. 2007, *ApJ*, 663, 866
- Dumas, G., Schinnerer, E., & Mundell, G. C. 2010, *ApJ*, 721, 911
- Elmegreen, B. G. 1994, *ApJ*, 425, 73
- Fathi, K., Storch-Bergmann, T., Riffel, R. A., Winge, C., Axon, D. J., Robinson, A., Capetti, A. & Marconi, A. 2006 *ApJ*, 641, 25
- Flower, D. R. & Launay, J. M. 1985, *MNRAS*, 241, 271
- Gao, Y., & Solomon, Philip M. 2004, *ApJ*, 606, 271
- Goldreich, P., & Kwan, J. 1974, *ApJ*, 189, 441
- Heckman, T. M. 1991, in *Massive stars in starbursts*, Eds: C. Leitherer, N. R. Walborn, T. M. Heckman, C. A. Norman, Cambridge Univ. Press
- Higdon, J. L. & Wallin, J. F. 2003, *ApJ*, 585, 281
- Ho, L. C., Filippenko, A. V. & Sargent, W. L. W. 1997, *ApJ*, 487, 591
- Ho, P. T. P., Moran, J. M., & Lo, F. 2004, *ApJ*, 616, L1
- Högbom, J. 1974, *ApJS*, 15, 417
- Hsieh, P.-Y., Matsushita, S., Lim, J., Kohno, K., & Sawada-Satoh, S. 2008, *ApJ*, 683, 70
- Hummel, E., van der Hulst, J. M., & Keel, W. C. 1987, *A&A*, 172, 32
- Kenney, J. D. P., Wilson, C. D., Scoville, N. Z., Devereux, N. A., & Young, J. S. 1992, *ApJ*, 395, 79
- Kennicutt, R. C. Jr. 1998, *ApJ*, 498, 541
- Kohno, K., Kawabe, R., & Vila-Vilaró, B. 1999, *ApJ*, 511, 157
- Kohno, K., Ishizuki, S., Matsushita, S., Vila-Vilaró, B., & Kawabe, R. 2003, *PASJ*, 55, L1
- Kotilainen, J. K., Reunanen, J., Laine, S., & Ryder, S. D. 2000, *A&A*, 353, 834
- Lada, E. A. 1992, *ApJ*, 393, 25
- Liu, G., Calzetti, D., Kennicutt, R. C., Jr., Schinnerer, E., Sofue, Y., Komugi, S., & Egusa, F. 2010a, in preparation
- Liu, G., Koda, J., Calzetti, D., Fukuhara, M., & Momose, R. 2010b, *ApJ*, in press
- Maloney, P. & Black J. H. 1988, *ApJ*, 325, 389
- Mazzuca, L. M., Knapen, J. H., Veilleux, S., & Regan, M. W. 2008, *ApJS*, 174, 337
- Meier, D. S., Turner, J. L. & Hurt, R. L. 2008, *ApJ*, 675, 281
- McKee, C. F., Storey, J. W. V., Watson, D. W., & Green, S. 1982, *ApJ*, 259, 647
- Meier, D. S., & Turner, J. L. 2001, *ApJ*, 551, 687
- Meier, D. S., Turner, J. L. & Hurt, R. L. 2008, *ApJ*, 675, 281
- Menéndez-Delmestre, K., Sheth, K., Schinnerer, E., Jarrett, T. H., & Scoville, N. Z. 2007, *ApJ*, 657, 790
- Onodera, S., et al. 2010, *ApJ*, 722, L127
- Muraoka K. et al. 2009, *ApJ*, 706, 1213
- Osterbrock, D. E. 1989, *Astrophysics of Gaseous Nebulae and Active Galactic Nuclei* (Research supported by the University of California, John Simon Guggenheim Memorial Foundation, University of Minnesota, et al.; Mill Valley, CA: University Science Books)
- Piner, B. G., Stone, J. M., Teuben, P. J. 1995, *ApJ*, 449, 508
- Petitpas, G. R., & Wilson, C. D. 2003, *ApJ*, 587, 649
- Rand, R. J. & Kulkarni, S. R. 1990, *ApJ*, 349, 43
- Reynaud, D., & Downes, D. 1997, *A&A*, 319, 737
- Sakamoto, K., Okumura, S. K., Ishizuki, S., Scoville, N. Z. 1999, *ApJ*, 525, 691
- Sakamoto, K., Ho, P. T. P., Mao, R.-Q., Matsushita, S., Peck, A. B. 2007, *ApJ*, 654, 782
- Sanders, D. B., Mazzarella, J. M., Kim, D.-C., Surace, J. A., & Soifer, B. T. 2003, *AJ*, 126, 1607
- Sandstrom, K. et al. 2010, *A&A*, 518, 59
- Schwarz, M. P. 1984, *MNRAS*, 209, 93
- Schinnerer, E., Böker, T., Emsellem, E., & Downes, D. 2007, *A&A*, 462, 27
- Scoville, N. Z., Soifer, B. T., Neugebauer, G., Matthews, K., Young, J. S. & Yerka, J. 1985, *ApJ*, 289, 129
- Scoville, N. Z., Yun, Min Su, Sanders, D. B., Clemens, D. P., & Waller, W. H. 1987, *ApJS*, 63, 821
- Solomon, P. M., Sanders, D. B., & Scoville, N. Z. 1979, *ApJ*, 232, 89
- Solomon, P. M., Rivilo, A. R., Barrett, J., & Yahil, A. 1987, *ApJ*, 319, 730
- Storch-Bergmann, T., Nemmen da Silva, R., Eracleous, M., Halpern, J. P., Wilson, A. S., Filippenko, A. V., Ruiz, M. T., Smith, R. C., & Nagar, N. M. 2003, *ApJ*, 598, 956
- Strong, A. W. & Mattox, J. R. 1996, *A&A*, 308, 21
- Telesco, C. M., & Gatley, I. 1981, *ApJ*, 247, 11
- Telesco, C. M., Dressel, L. L., & Wolstencroft, R. D. 1993, *ApJ*, 414, 120
- Toomre, A. 1964, *ApJ*, 139, 1217
- Tosaki, T., Shioya, Y., Kuno N., Hasegawa, T., Nakanishi, K., Matsushita, S. & Kohno, K. 2007 *PASJ*, 59, 33
- Tully, R. B. 1988, *Nearby Galaxies Catalog* (Cambridge: Cambridge University Press)
- van de Ven, G. & Fathi, K. 2010 *ApJ*, 723, 767
- Verley, S., Corbelli, E., Giovanardi, C., & Hunt, L. K. 2010, *A&A*, 510, 64
- Vogel, S. N., Kulkarni, S. R., & Scoville, N. Z. 1988, *Nature*, 334, 402
- Wada, K., & Norman, C. A. 2002, *ApJ*, 566, L21
- Wild, W. et al. 1992, *A&A*, 265, 447
- Williams, J. P., de Geus, E. J., & Blitz, L. 1994, *ApJ*, 428, 693
- Young, J. S. & Scoville, N. Z. 1991, *ARA&A*, 29, 581

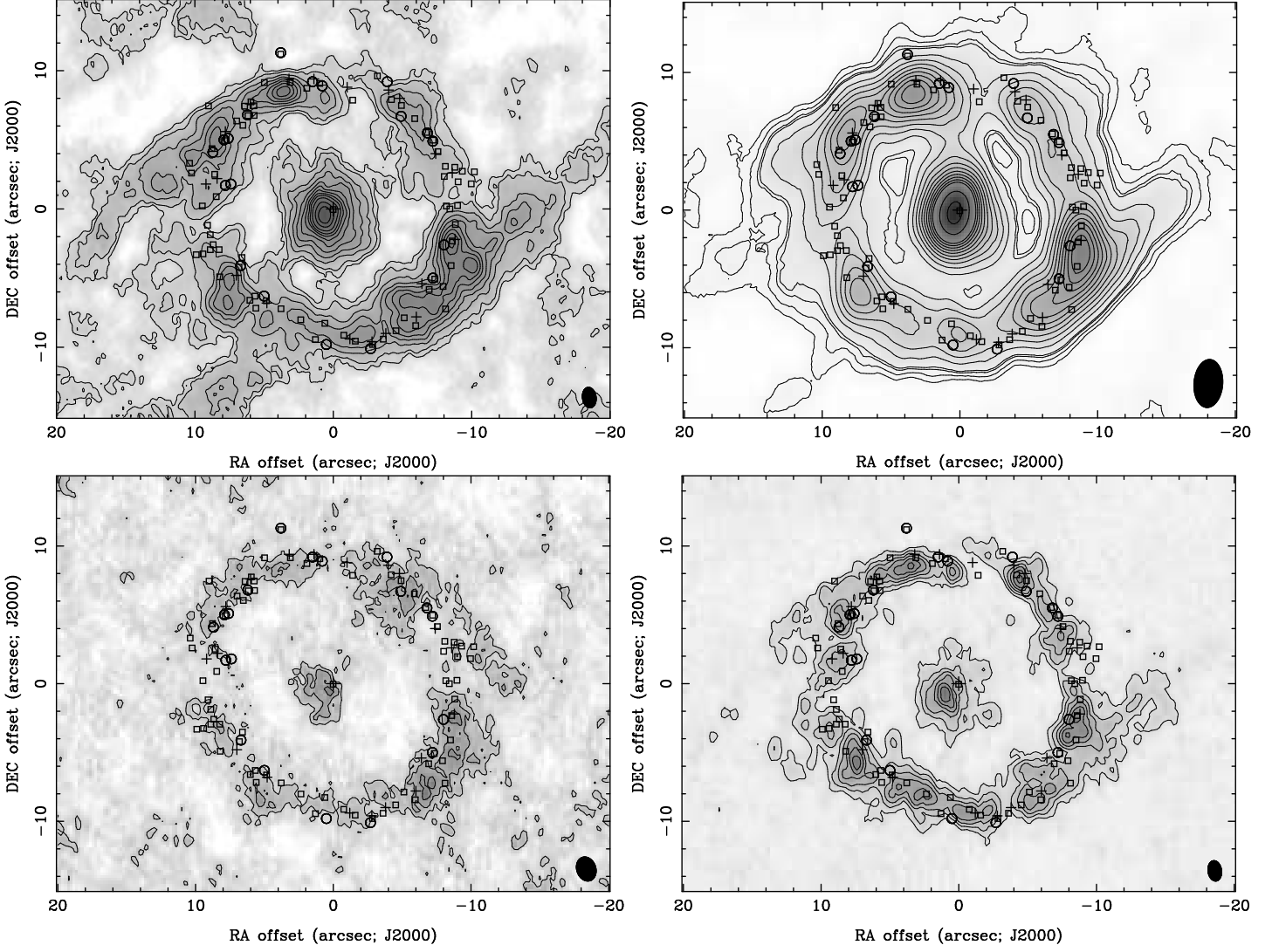


Figure 1. Top left image is the $^{12}\text{CO}(J = 2-1)$ integrated intensity map. The contour levels are 2, 3, 5, ..., 20, 25, and 30σ ($1\sigma = 2.3 \text{ Jy km s}^{-1} \text{ beam}^{-1}$). The synthesized beam is $1''.5 \times 1''.0$ (PA = $8^\circ 1$). The emission at $(10'', -15'')$ are sidelobes. Top right image is the $^{12}\text{CO}(J = 3-2)$ integrated intensity map. The contour levels are 5, 7, 9, 10, 15, ..., 60, 80, and 100σ ($1\sigma = 3.0 \text{ Jy km s}^{-1} \text{ beam}^{-1}$). The synthesized beam is $3''.5 \times 2''.1$ (PA = $-4^\circ 4$). Bottom left image is the $^{13}\text{CO}(J = 2-1)$ integrated intensity map. The contour levels are 2, 3, and 4σ ($1\sigma = 2.1 \text{ Jy km s}^{-1} \text{ beam}^{-1}$). The synthesized beam is $1''.8 \times 1''.4$ (PA = 19°). Bottom right image is the $^{12}\text{CO}(J = 2-1)$ peak brightness temperature map. The contours are 2, 3, 4, 5, 6, and 7 K. All of the maps are overlaid with the positions of Pa α star clusters (squares), 6 cm radio continuum sources (crosses), and V-band ($< 13 \text{ mag}$) star clusters (circles). The central cross in each map is the position of the 6-cm nucleus (Hummel et al. 1987), which is assumed to be the active nucleus. The beam size is shown in the lower right corner of each map.

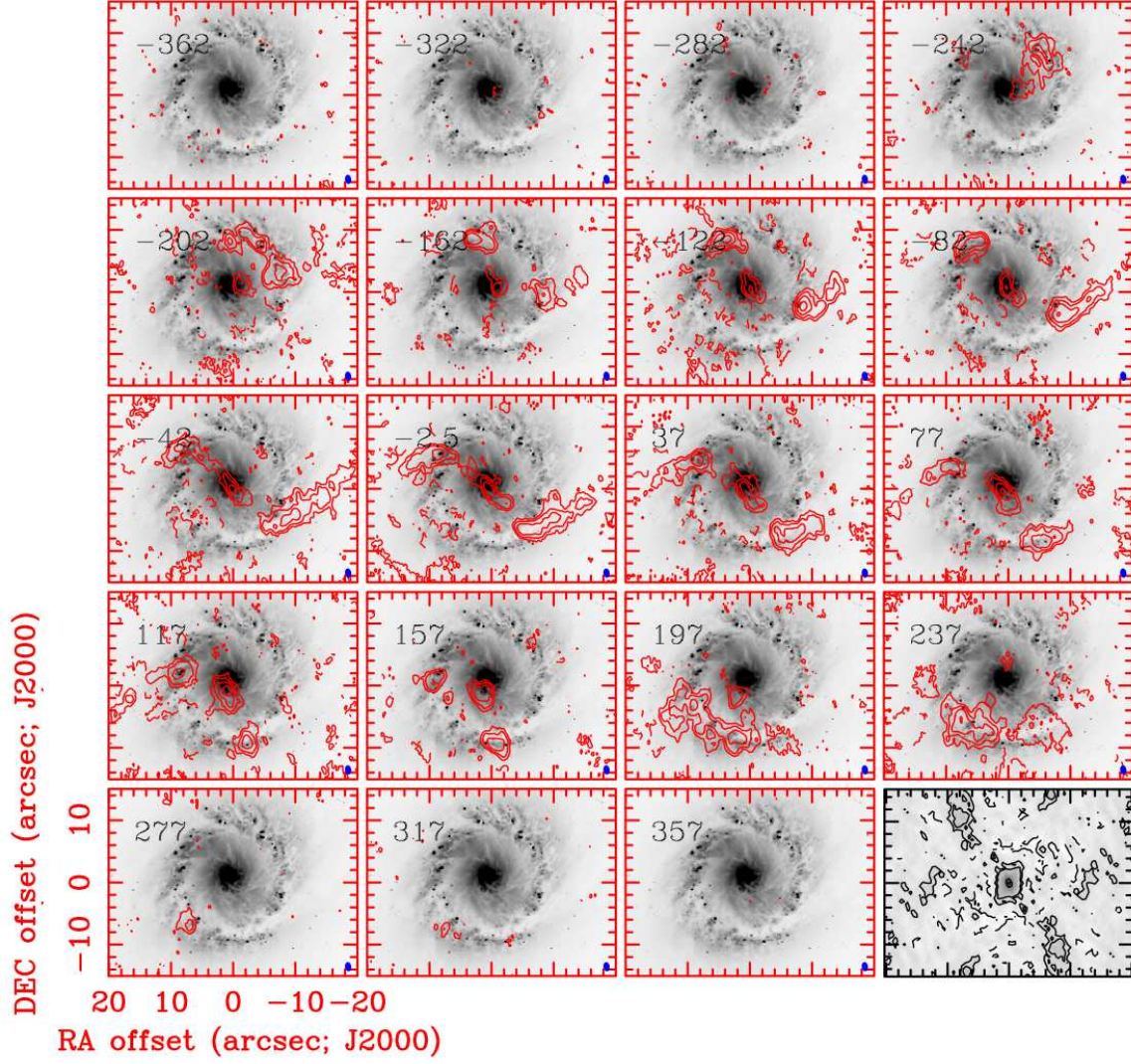


Figure 2. The $^{12}\text{CO}(J = 2-1)$ channel maps are overlaid on the archival HST I-band (F814W) image with the corrected astrometry. The contour levels are $-2, 2, 4, 8, 16$, and 32σ , where $1\sigma = 20 \text{ mJy beam}^{-1}$ (306 mK) in 40 km s^{-1} resolution. The velocity (km s^{-1}) with respect to the systemic velocity of 1254 km s^{-1} (Kohno et al. 2003) is labeled in the top left corner of each map. The beam size ($1''.5 \times 1''.0$, $\text{PA} = 8^\circ.1$) is shown in the lower right corner of each map with solid ellipse. The dirty beam is at the bottom right panel with a contours level of $-100, -50, -10, -5, 5, 10, 50, 100\%$ of the peak.

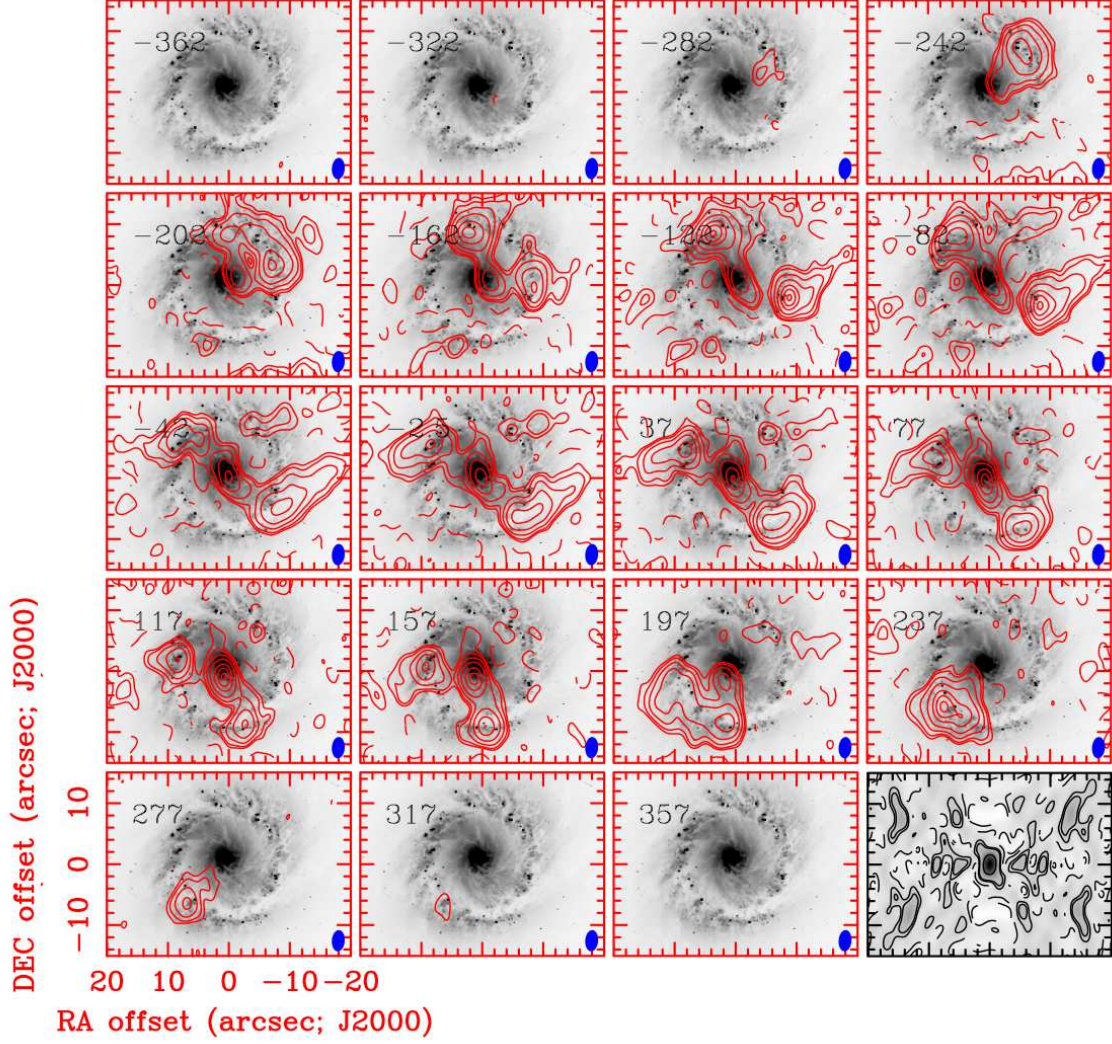


Figure 3. The $^{12}\text{CO}(J = 3-2)$ channel maps are overlaid on the archival HST I-band (F814W) image with the corrected astrometry. The contour levels are -3, 3, 5, 10, 20, 40, 60, and 80σ , where $1\sigma = 17.5 \text{ mJy beam}^{-1}$ (23 mK) in 40 km s^{-1} resolution. The velocity (km s^{-1}) with respect to the systemic velocity of 1254 km s^{-1} is labeled in the top left corner of each map. The beam size ($3''.5 \times 2''.1$, $\text{PA} = -4^\circ.4$) is shown in the lower right corner with solid ellipse. The dirty beam is at the bottom right panel with a contours level of -100, -50, -10, -5, 5, 10, 50, 100% of the peak.

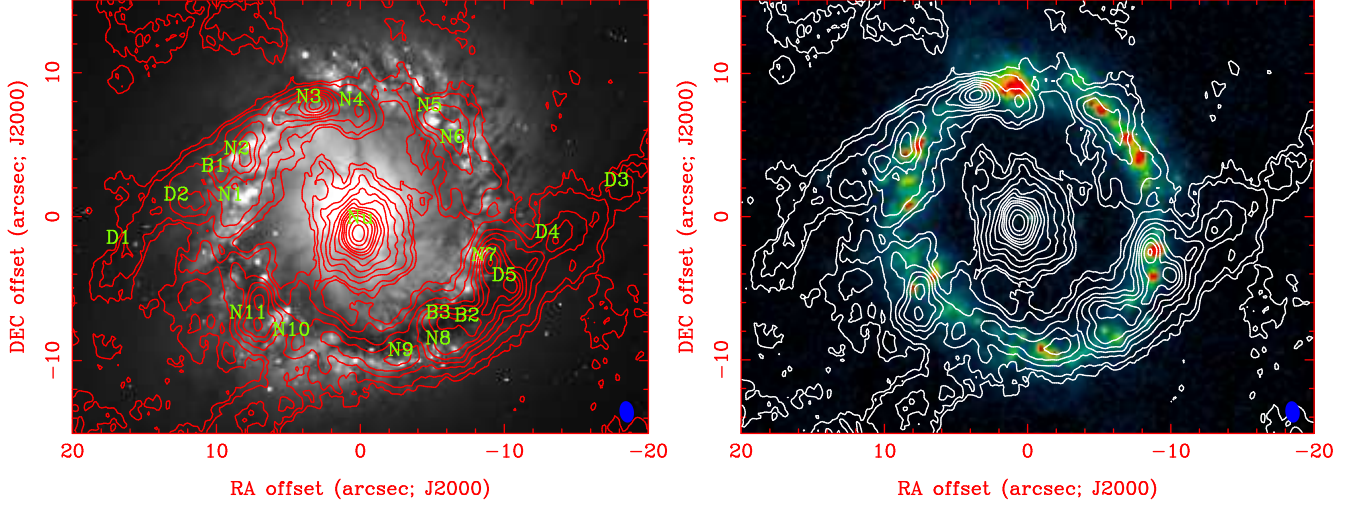


Figure 4. Top image is the $^{12}\text{CO}(J=2-1)$ integrated map (contours) overlaid on the archival HST I-band (Filter F814 W) image (grey scale). Astrometry of the HST image was corrected using background stars with known positions. The contour levels for the $^{12}\text{CO}(J=2-1)$ are 2, 3, 5, ..., 20, 25, and 30σ ($1\sigma = 2.3 \text{ Jy km s}^{-1} \text{ beam}^{-1}$). The IDs for the individual peaks of clumps are marked. The CO synthesized beam ($1''.5 \times 1''.0$) is shown in the lower right corner. Bottom image is the HST NICMOS Pa α line image (color) overlaid on the $^{12}\text{CO}(J=2-1)$ contour. The contour levels are the same as in upper image.

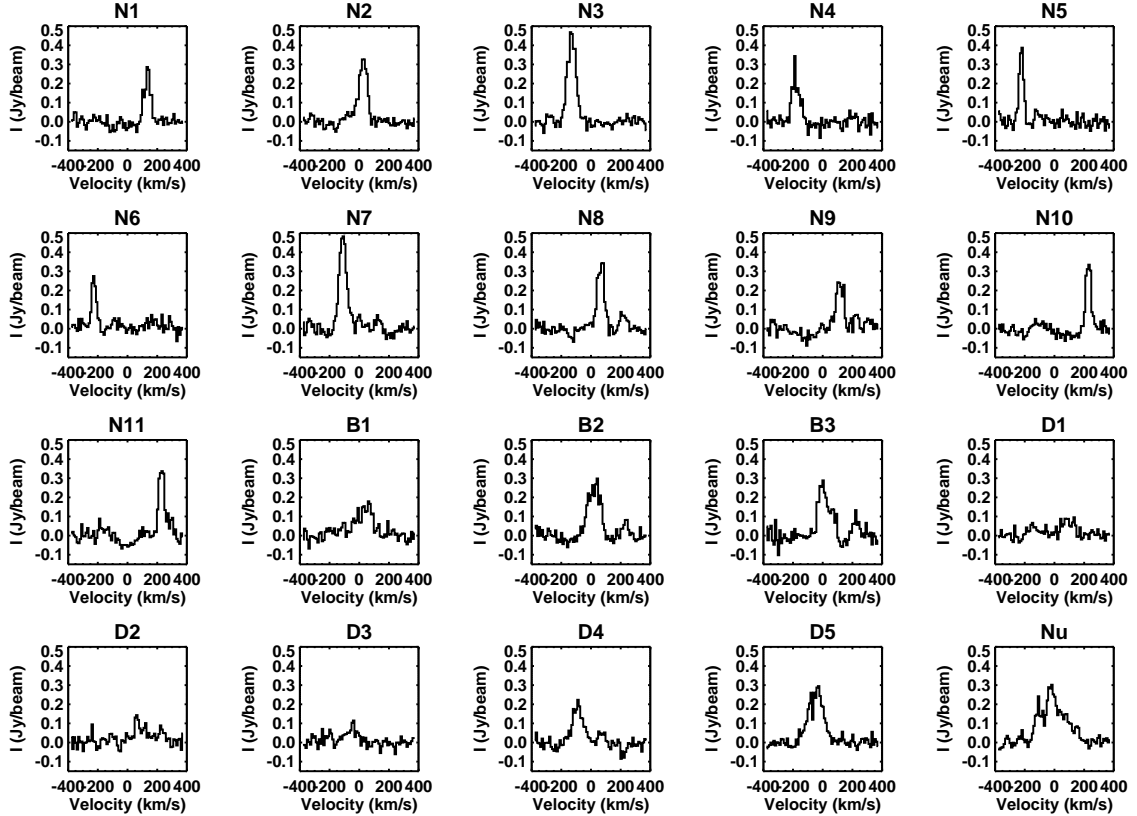


Figure 5. The high resolution ($1''.5 \times 1''.0$) $^{12}\text{CO}(J=2-1)$ spectra of individual clumps measured at the $^{12}\text{CO}(J=2-1)$ peak position within one beam. The velocity is relative to the systemic velocity of 1254 km s^{-1} and spectral resolution is 10 km s^{-1} . The IDs of the clumps are labeled in each panel.

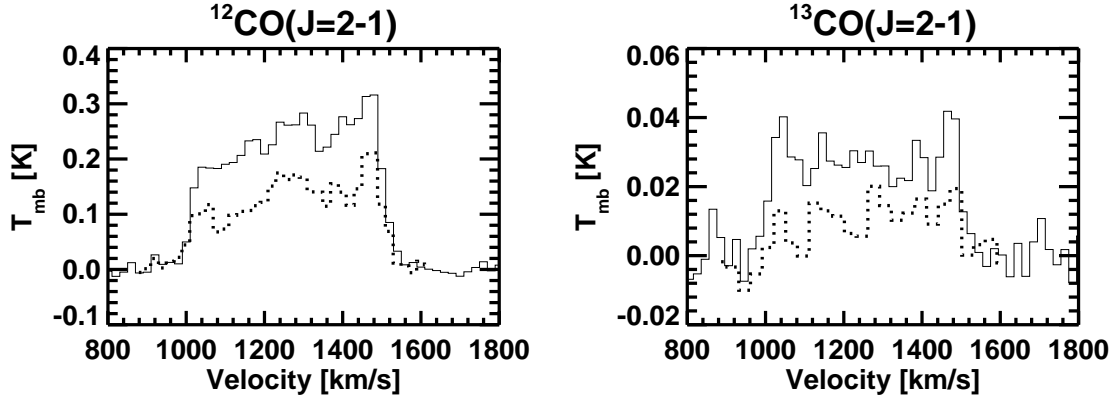


Figure 6. Left: We show the $^{12}\text{CO}(J = 2-1)$ spectra, where the solid line is the JCMT data (Petitpas et al. 2003) and the dotted line is our SMA data. The intensity scale is the main beam temperature at $21''$ resolution. We only took 6 chunks to make the SMA maps, so the velocity range is smaller than that of JCMT. Right: The $^{13}\text{CO}(J = 2-1)$ spectra, where the solid line is the JCMT data, and the dotted line is our SMA data. The beam size of the two data are matched to $21''$.

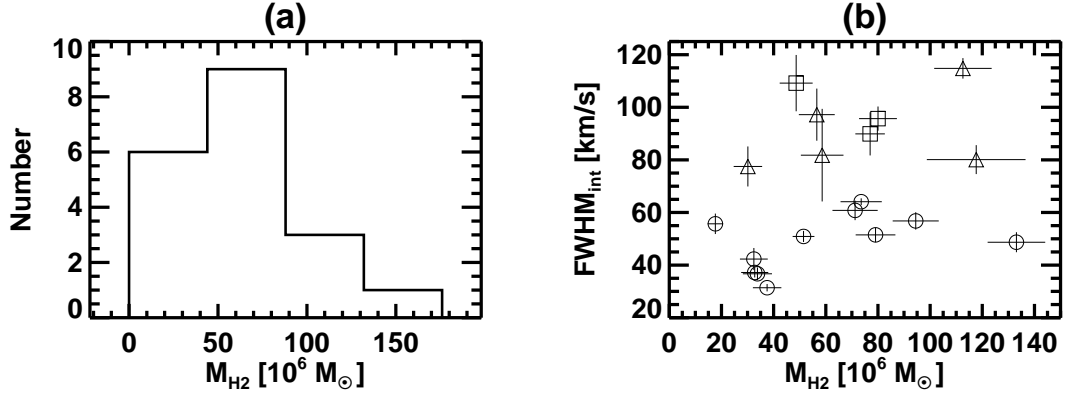


Figure 7. (a) The number histogram of the total H_2 mass of the clumps in the ring. Horizontal and vertical axis are the gas mass and number, respectively. The gas mass is in units of $10^6 M_{\odot}$. The negative horizontal axis is to show the plot clearly. (b) The correlation between total H_2 mass and FWHM intrinsic line width of the narrow line ring clumps (circles), broad line ring clumps (squares), and dust lane clumps (triangles). The H_2 mass is in units of $10^6 M_{\odot}$. The uncertainties of $\pm 1\sigma$ are overlaid on the symbols with vertical/horizontal bars.

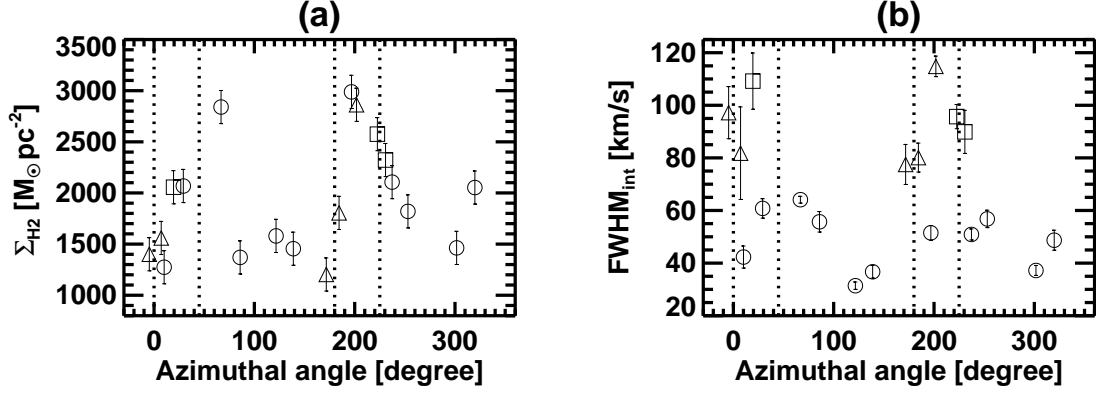


Figure 8. (a) Σ_{H_2} measured at the position of the intensity peak in units of $\text{M}_{\odot} \text{pc}^{-2}$ (see Table 2) as a function of azimuthal angle. East direction corresponds to 0° , and increase is in clockwise direction. The dashed lines mark position angle from 0° to 45° and from 180° to 225° , which roughly correspond to the position of the orbit crowding regions. The meaning of the symbols are the same as in Figure 7b. (b) The FWHM intrinsic line width of clumps as a function of azimuthal angle. The dashed lines are the same as in (a). The uncertainties of $\pm 1\sigma$ are overlaid on the symbols with vertical/horizontal bars.

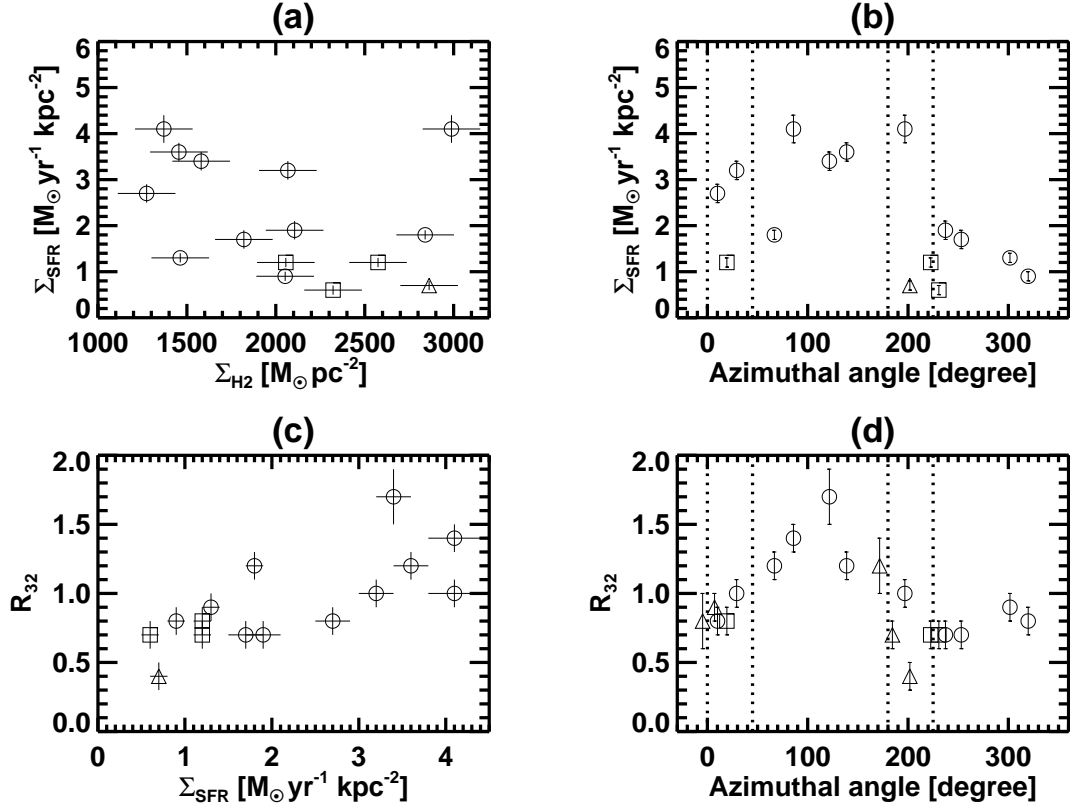


Figure 9. (a) Surface SFR density ($\text{M}_{\odot} \text{yr}^{-1} \text{kpc}^{-2}$) is shown as a function of Σ_{H_2} ($\text{M}_{\odot} \text{pc}^{-2}$). The symbols are the same as in Figure 8. The meaning of the symbols are the same as in Figure 7b. (b) Surface SFR density is shown as a function of azimuthal angle. The dashed lines mark position angle from 0° to 45° and from 180° to 225° . (c) Surface SFR density ($\text{M}_{\odot} \text{yr}^{-1} \text{kpc}^{-2}$) is shown as a correlation of R_{32} . (d) R_{32} is shown as a function of azimuthal angle. The uncertainties of $\pm 1\sigma$ are overlaid on the symbols with vertical/horizontal bars.

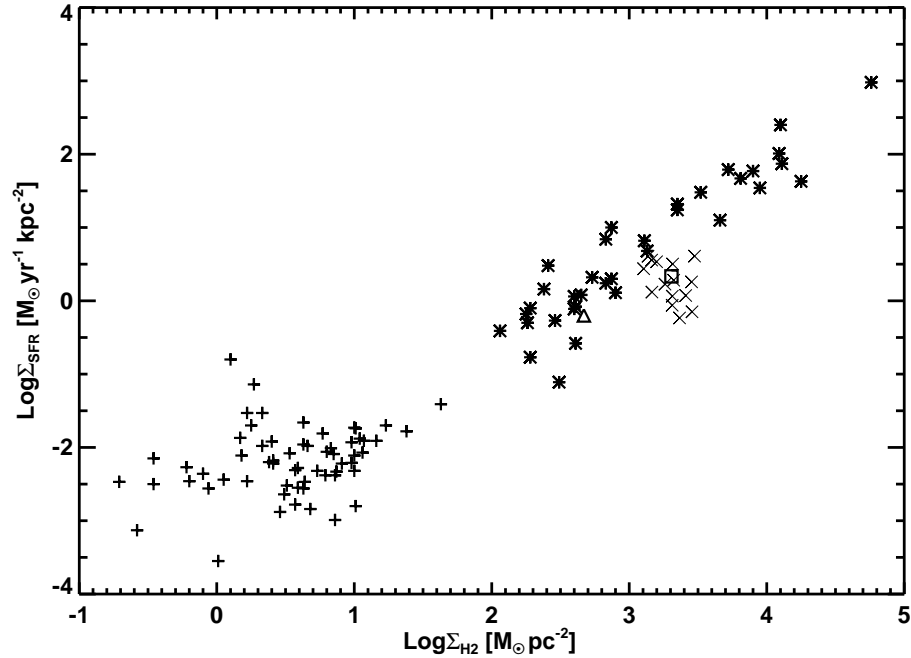


Figure 10. The correlation of Σ_{H_2} and surface SFR density of individual clumps of NGC 1097 are overlaid on the data used in Kennicutt (1998). Their data for normal galaxies are represented as plus signs, and infrared-selected circumnuclear starburst galaxies as asterisks, while their NGC 1097 data point is marked as triangle. Our spatially resolved clumps of the circumnuclear starburst ring of NGC 1097 are marked as crosses, and the average value of the clumps is marked as a square.

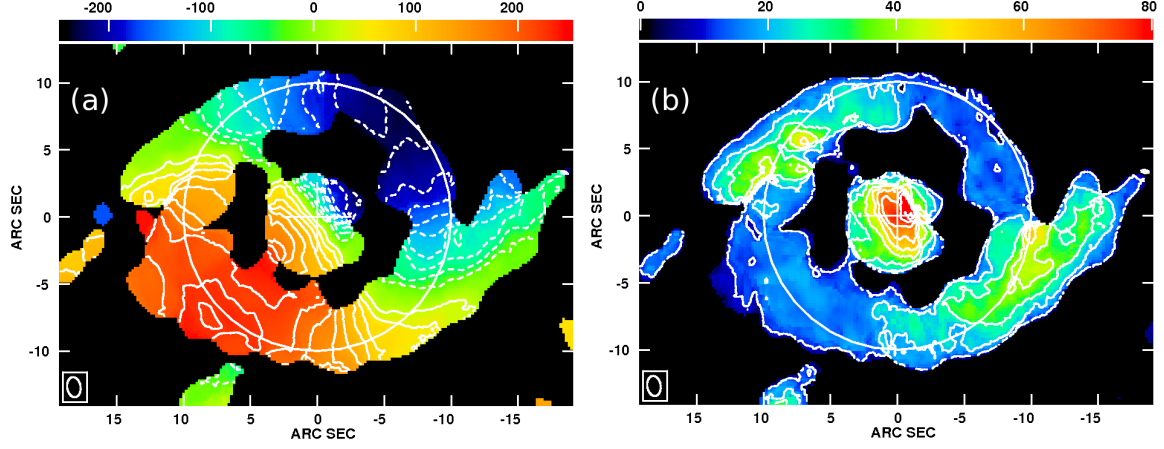


Figure 11. (a) The intensity weighted mean velocity map (MOM1) of $^{12}\text{CO}(J = 2-1)$ line with respect to the systematic velocity (1254 km s^{-1}), solid and dashed lines represent the redshifted and blueshifted velocity respectively. The first negative contour (close to the central cross) is 0 km s^{-1} , and the contour spacing is in 25 km s^{-1} resolution. (b) The intensity weighted velocity dispersion map (MOM2). The contour interval is 10 km s^{-1} , note the values are not FWHM line width but the square root of the dispersion relative to the mean velocity. Therefore the number is lower than the FWHM we derived by line fitting.

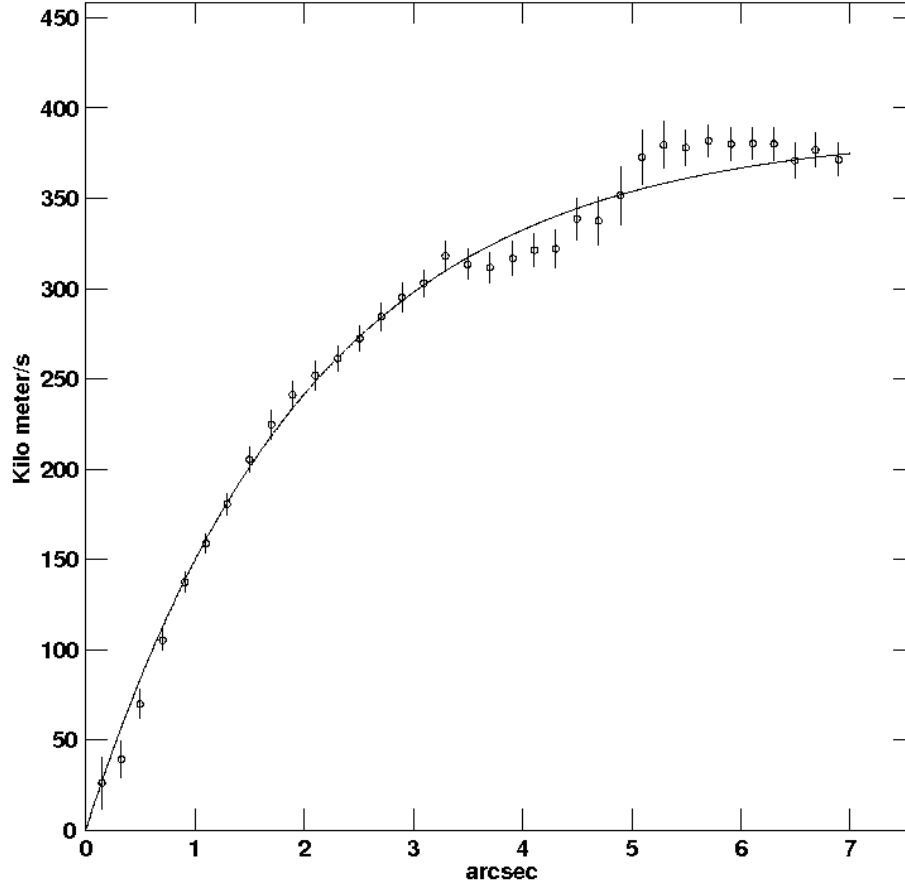


Figure 12. We show the data of rotation curve (circles) of NGC 1097 overlaid with the fitted curve (solid line) in GAL.

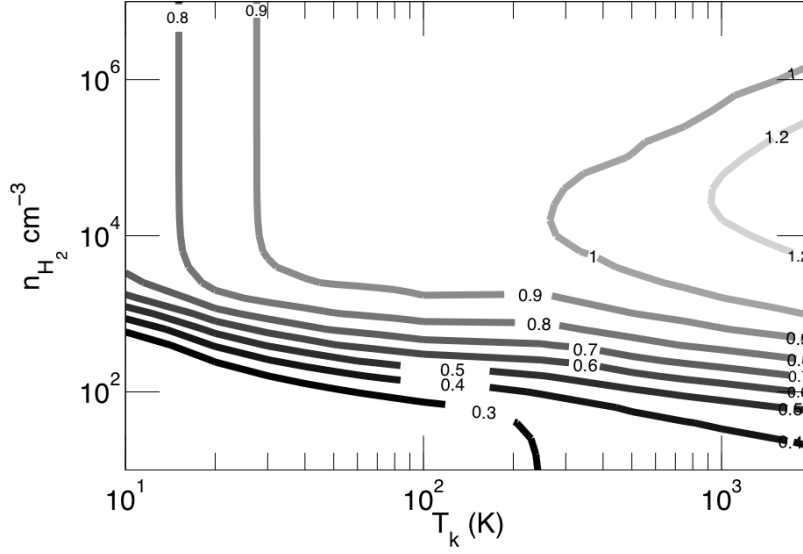


Figure 13. The LVG calculations of the R_{32} is shown as a function of kinetic temperature and H_2 number density. The R_{32} are labeled on the contours.

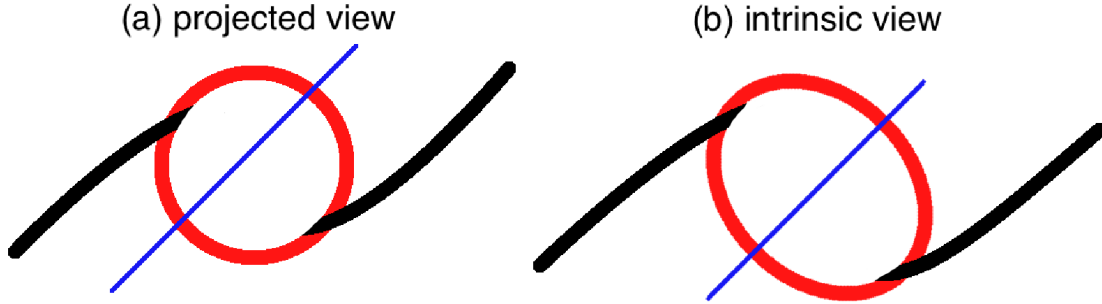


Figure 14. The cartoon sketch of the gas morphology in the circumnuclear region of NGC 1097. The red circle represents the starburst ring, where the narrow line clumps are located. The black curves are the dust lane associated with shock wave, where the broad line clumps are located. The blue line is the major axis of the large scale stellar bar. We show: (a) the projected view of the morphology of the starburst ring/dust lane associated with our observation. It shows a nearly circular starburst ring. (b) the intrinsic shape of the ring, which is expected to be an ellipse.